be more optimal than ChR2 to depolarize exogenously expressed cells by light.

EXPERIMENTAL PROCEDURES

Plasmid Construction and Expression—The cloning methods of channelopsin1 (chop1) have been described previously (8). Chimeric channelopsins (chops)[2] between chop1 (amino acids 1–345; GenBank[TM] accession numbers, AB058890/AF385748) and chop2 (amino acids 1–315) (GenBank[TM] accession number, AB058891/AF461397) with 5′-EcoRI and 3′-BamHI restriction sites were constructed by overlap extension PCR as described previously (15) using KOD plus DNA polymerase (Toyobo, Osaka, Japan). A chimeric chop fragment was obtained, purified, digested by EcoRI and BamHI, and subcloned in-frame into the plasmid pVenus-N1 that has the Venus construct (14). Single amino acid mutants of chop2-(1–315)-Venus were produced using KOD plus mutagenesis kit (Toyobo). Primers used in overlap extension and site-directed mutagenesis are listed in supplemental data 1. Coding regions in all constructed plasmids were fully sequenced to verify that no undesired mutations had been introduced by PCR. HEK293 cells were cultured at 37 °C and 5% CO_2 in Dulbecco's modified Eagle's medium (Sigma) supplemented with 10% fetal bovine serum and transfected using Effectene transfection reagent (Qiagen, Tokyo, Japan) according to the manufacturer's instructions. Twenty four hours post-transfection, the cells were replated onto the collagen-coated glass coverslips and served for the electrophysiology. We did not supplement the culture and experimental media with retinal, but we observed enough large photocurrents for the following experiments.

Measurements of Fluorescence—Cells were prepared for electrophysiological recordings 48 h after transfection. Under conventional confocal microscopy (LSM 510 META, Carl Zeiss, Oberkochen, Germany), Venus was excited at 488 nm, and the fluorescence was obtained with an LP505 emission filter. All the images were captured under fixed conditions such as the laser power and the photomultiplier gain so as to compare the fluorescence distribution among the ChR2 variants. The fluorescence derived from the contour of a cell was automatically detected by an algorithm (supplemental data 2) and then measured in arbitrary fluorescent units. This value was normalized by the number of pixels in the region, and the fluorescence density was obtained.

Electrophysiology—The current-voltage (*I–V*) relationship was examined 48 h after transfection to compare the effective conductance with the membrane protein expression. Other experiments were done 48–96 h after transfection. Fluorescence-labeled isolated cells were identified under conventional epi-fluorescence microscopy (BH2-RFC, Olympus, Tokyo, Japan) equipped with a 60× water-immersion objective (LUMplanPl/IR60x, Olympus). The photocurrents were recorded under the whole-cell patch clamp of a conventional system (Axopatch 200A plus Digdata1200, Molecular Devices Co., Sunnyvale, CA). The standard patch pipette solution contained (in mM), 120 CsOH, 100 glutamate, 50 HEPES, 2.5 MgCl,

2.5 MgATP, 5 Na_2EGTA, 1.2 leupeptin (Sigma), pH 7.4, adjusted by 1 N CsOH. For the analysis of the *I–V* relationship, Cs^+ was replaced by isomolar Na^+. The access resistance was 10–20 megohms and was monitored throughout the recording. The cells were continuously superfused (1–2 ml/min) by standard Tyrode solution (in mM, 138 NaCl, 3 KCl, 1 $CaCl_2$, 1 $MgCl_2$, 10 HEPES, NaOH 4, pH 7.4, by 1 N HCl) or low Na^+ Tyrode solution (in mM, 16 NaCl, 3 KCl, 1 $CaCl_2$, 1 $MgCl_2$, 122 N-methyl-D-glucamine, 122 HCl, 10 HEPES, 4 NaOH). The liquid junctional potentials of the sodium glutamate patch pipette were -8 mV at 142 mM Na^+ and -14 mV at 20 mM Na^+ and were corrected. All experiments were performed at room temperature (22–25 °C).

Light Illumination—Three modes of light illumination were used according to the experiments. For the wavelength-response relationship monochromatic light at 400–560 nm (width, 10 nm) of 1-s duration was applied every 20 s under a conventional epifluorescence system equipped with a xenon lamp and electromagnetic shutter (CAM-230, Jasco, Tokyo, Japan). Usually the photocurrent was measured by 2–3 repeats of a protocol, in which the wavelength was changed in the order of 460, 480, 500, 520, 540, 560, 560, 540, 520, 500, 480, 460, 440, 420, 400, 400, 420, 440, and 460 and was averaged for each wavelength. The power density at each wavelength was directly measured by a thermopile (*MIR-100Q*, Mitsubishi Oil Chemicals, Tokyo, Japan), and was (in mW mm^{-2}) 0.021 (400 nm), 0.018 (420 nm), 0.027 (440 nm), 0.027 (460 nm), 0.018 (480 nm), 0.021 (500 nm), 0.015 (520 nm), 0.014 (540 nm), or 0.012 (560 nm), respectively. To investigate the wavelength-response relationship, the amplitude of the peak photocurrent at each wavelength was divided by the power density because there was assumed to be a linear relationship between these values (14). For the *I–V* relationship analysis the xenon lamp light was filtered at 477 ± 10 nm (power density, 1.6 mW mm^{-2}) and was applied for 0.2 s duration every 10 s under a conventional epifluorescence system equipped with an electromagnetic shutter (OSP-3, Olympus). For the analysis of the photocurrent kinetics, we used a blue LED (470 ± 25 nm, LXHL-NB98, Lumileds Lighting Inc., San Jose, CA) regulated by a pulse generator (SEN-7203, Nihon Kohden, Tokyo, Japan) and computer software (pCLAMP 9, Molecular Devices Co.). The maximal power density of LED light was 0.077 mW mm^{-2}.

Data Analysis—The desensitization was quantified as the difference between the peak and the steady-state amplitudes divided by the peak amplitude. The time constants of turning-on (ON) transition (ON time constant, τ_{ON}) were obtained by fitting the photocurrent using the simplex method of nonlinear least squares protocol of the appropriate software (Clampfit 9.2 and 10.1, Molecular Devices Co.). Because the photocurrent was better fitted by two exponential functions after light-off, the effective turning-off (OFF) time constant (τ_{OFF}) was measured as the time to reach e^{-1} (37%) of the steady-state amplitude.

All data in the text are presented as means ± S.E. (number of observations). Mann-Whitney *U* test was used for statistical analysis unless otherwise noted. According to this *p* value, the statistical significance was scored as 0 if $p > 0.05$, as 1 if $0.05 > p > 0.01$, as 2 if $0.01 > p > 0.005$, as 3 if $0.005 > p > 0.001$, as 4

---

[2] The abbreviations used are: chop, channelopsin; mW, milliwatt; S, siemens; F, farad.
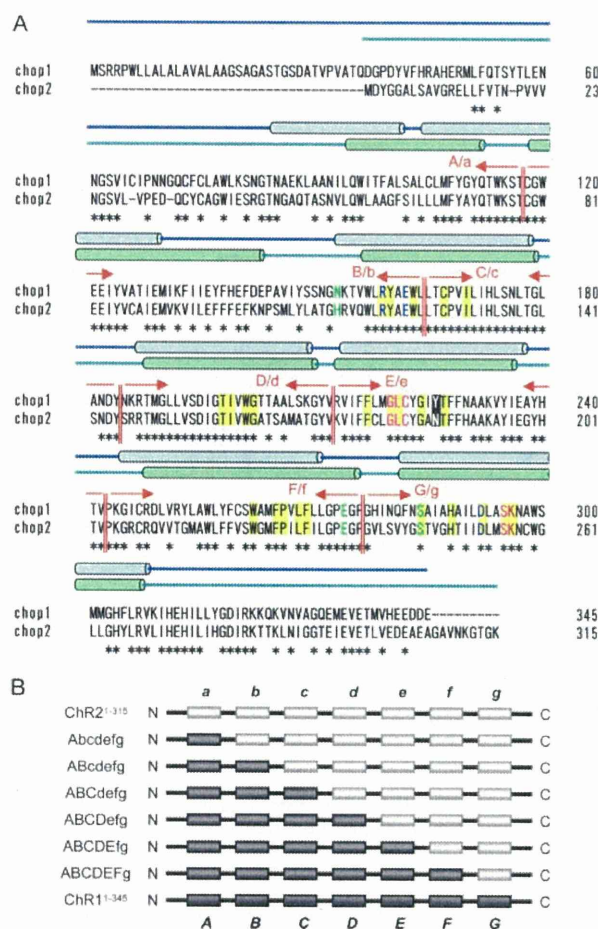
A

B

FIGURE 1. **Primary structure of channelopsin chimeras.** *A*, sequence alignment of two channelrhodopsin apoproteins, channelopsin1 (chop1, amino acids 1–345) and channelopsin2 (chop2, amino acids 1–315). The identical amino acids are indicated with an *asterisk*. The putative seven transmembrane domains are indicated by *blue cylinders* (16, 17) or *green cylinders* (8). *Yellow background* indicates the amino acid residues predicted to lie close to retinal. *Crimson letters* indicate the consensus retinal-binding Lys. *Blue letters* indicate the consensus residues defining the Schiff base counterion complex. *Magenta letters* indicate the amino acid residues involved in the retinal-Schiff base binding pocket. *Green letters* indicate the amino acid residues affecting the electron distribution of retinal-Schiff base. Tyr[226]("E")/Asn[187]("e"), which are involved in both the wavelength preference and channel gating, are shown by *white letters* with *black background*. *Vertical red double lines* indicate the segment boundaries. The segments are named from the N-terminal as "A" to "G" of chop1 and as "a" to "g" of chop2. *B*, primary constructs of the chimera channelrhodopsins replacing the N-terminal segments of channelrhodopsin2 (ChR2-(1–315)) with homologous counterparts of channelrhodopsin1 (ChR1-(1–345)).

if $0.001 > p > 0.0005$, as 5 if $0.0005 > p > 0.0001$, and as 6 if $p < 0.0001$.

RESULTS

Replacement of N-terminal Segments of ChR2 with Homologous Counterparts of ChR1—Previous studies suggested that ChR1 and -2 have distinct properties, although these apoproteins are highly homologous (Fig. 1A). The first to seventh transmembrane domains for each are predicted, although the amino acid sequence involved in the domain was somewhat different among several studies (8, 16, 17). We divided the N-terminal 1–345 amino acids fragment of ChR1 apoprotein (channelopsin1, chop1), which is essential to the photocurrent

activation (18), into seven segments so that each, as much as possible, would contain one of the transmembrane domains. These segments are referred to (from N-terminal to C-terminal) as "A," "B," "C," "D," "E," "F," and "G." The homologous counterparts of the essential truncate (1–315 amino acids) of ChR2 apoprotein (channelopsin2, chop2) (11), are referred to as "a," "b," "c," "d," "e," "f," and "g." To identify the segment differentiating the ChR2 photocurrent properties from the ChR1, the N-terminal segments of ChR2-(1–315) were replaced by the homologous counterparts of ChR1-(1–345). We thus made six chimera channelrhodopsins as follows: ChR(Abcdefg), ChR(ABcdefg), ChR(ABCdefg), ChR(ABCDefg), ChR(ABCDEfg), and ChR(ABCDEFg) (Fig. 1B).

Membrane Expression—These channelrhodopsins were tagged with one of the green fluorescent protein derivatives, Venus, at their C-terminal ends and expressed in HEK293 cells. Under confocal microscopy, ChR2-(1–315)-Venus fluorescence was distributed preferentially at the contour of the cell, suggesting that it is distributed in the plasma membrane (Fig. 2A). Although the fluorescence was weak in the cases of ChR1-(1–345), it was again preferentially distributed at the contour of the cell. The expression was obviously enhanced in any case of chimera channelrhodopsin. As shown in Fig. 2B, the fluorescence density in the plasma membrane region was quantified and compared among ChR2-(1–315), ChR1-(1–345), and chimera channelrhodopsins. The fluorescence density of ChR-(Abcdefdg) was similar to ChR2, whereas those of ChR(ABcdefg), ChR(ABCdefg), ChR(ABCDefg), and ChR(ABCDEfg) were 150–200% of ChR2. The further "f"-to-"F" exchange significantly reduced the fluorescence density but to a level as great as that of ChR2-(1–315). In contrast, the fluorescence density of ChR1-(1–345) was very small. This result was generally consistent with the immunoblot quantification of membrane-targeted proteins, although the immunoblot density of ChR1-(1–345) was similar to that of ChR(ABCDEFg) (supplemental data 3). Therefore, the fluorescence density at the contour of the cell would well represent the density of the molecule at the plasma membrane.

Reevaluation of ChR1 Photocurrent at pH 7.4—Because the ChR1 photocurrent has been studied at pH 4–6 in previous studies (10, 18), its properties at pH 7.4 were re-investigated. Under whole-cell patch clamp at −40 mV, a 1-s light pulse evoked a negative ChR1-(1–345) current with negligible desensitization at wavelengths of 460 and 520 nm (Fig. 3A), whereas the same light pulse evoked a ChR2-(1–315) current with a peak and a plateau, both of which were dependent on the wavelength (Fig. 3B). For each, the photocurrents were evoked at wavelengths of 400–560 nm. Because the light power was dependent on the wavelength, it was measured directly and was in the range of 0.012–0.027 mW mm^{-2}. The peak photocurrent was almost proportional to the light power density in this small value range (14). The photocurrent sensitivity to each wavelength was thus obtained by dividing the peak photocurrent amplitude by the light power density and normalized to the value at 480 nm. The sensitivity was maximal between 480 and 520 nm in the case of ChR1-(1–345) (Fig. 3C). This sensitivity-wavelength relationship was almost identical to the sensitivity-wavelength relationship of ChR1 at pH 7.5 (13). On the other
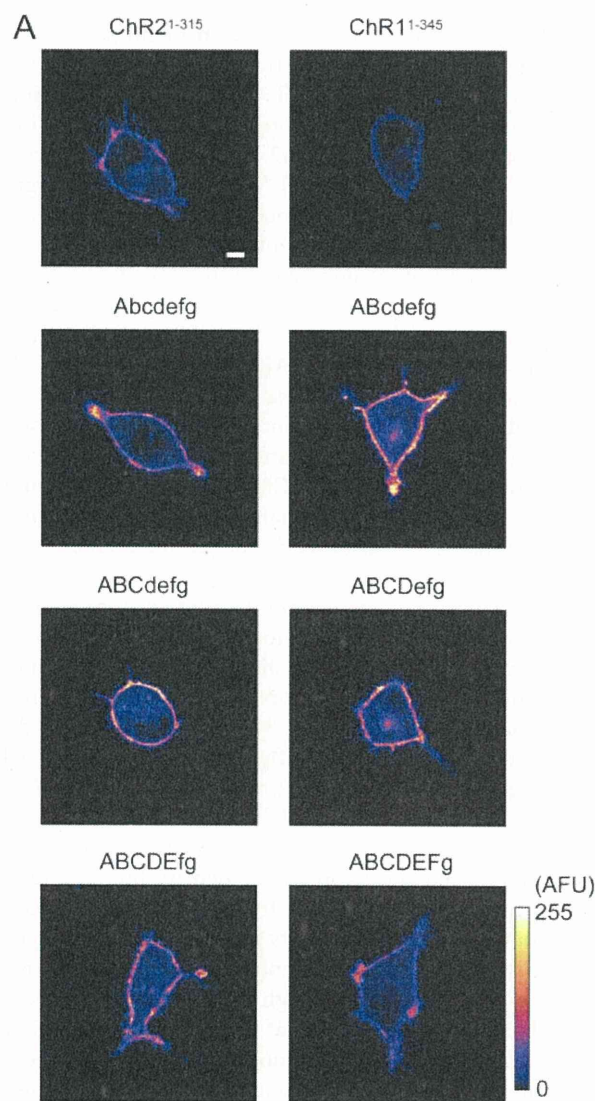
FIGURE 2. **Plasma membrane expression.** *A,* confocal images of the representative HEK293 cells expressing each channelrhodopsins. *Scale bar,* 5 μm. The fluorescence intensity was scaled by the arbitrary fluorescent unit (*AFU*) and expressed in pseudocolor ratings. *B,* average fluorescence densities (mean ± S.E.) at the cell contour of ChR2-(1–315), chimeras and ChR1-(1–345). In this and the following *bar graphs* the number of experiments is in *parentheses,* and the *number with an asterisk* indicates the significance score (Mann-Whitney *U* test).
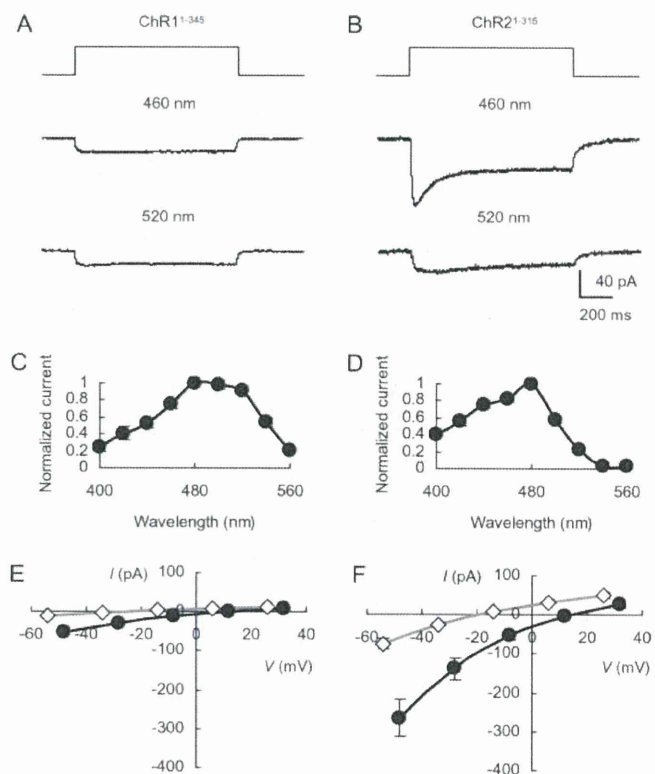

FIGURE 3. **Comparison of photocurrents.** *A,* sample ChR1-(1–345) photocurrent evoked by 1-s pulse illumination (*top*) at 460 nm (*middle*) or 520 nm (*bottom*). *B,* similar to *A,* but a ChR2-(1–315) photocurrent. *C,* wavelength relationship of the ChR1-(1–345) photocurrent ($n = 8$). Mean ± S.E. of normalized currents to 480 nm. *D,* wavelength relationship of the ChR2-(1–315) photocurrent ($n = 8$). *E,* current-voltage (*I-V*) relationships of the ChR1-(1–345) photocurrent at 142 mM [Na$^+$]$_o$ (*filled circles,* mean ± S.E.) and 20 mM [Na$^+$]$_o$ (*open diamonds,* mean ± S.E.). *F, I-V* relationship of the ChR2-(1–315) photocurrent.

hand, in the case of ChR2-(1–315), the sensitivity at 500–520 was smaller than that at 480 nm (Fig. 3D).

The ChR1-(1–345) photocurrents were usually small in comparison with the ChR2-(1–315) as noted in Fig. 3, *A* and *B*. The current-voltage (*I-V*) relationship was investigated for each peak photocurrent evoked by blue light (477 ± 10 nm), which is the wavelength at the maximal sensitivity for both ChR1-(1–345) and ChR2-(1–315), with a pipette solution containing 120 mM Na$^+$. When the extracellular solution was the standard Tyrode solution containing 142 mM Na$^+$, the *I-V* relationships of ChR1 and ChR2 were slightly rectified inwardly as shown in Fig. 3, *E* and *F, i.e.* the slope conductance at positive membrane potentials was smaller than that at negative membrane potentials. Under close inspection, the ChR2 photocurrent was more rectified than the ChR1 one (supplemental data 4). To evaluate the size of the photocurrent, we estimated the effective conductance as a slope of the *I-V* relationship between −40 and 40 mV divided by the input capacitance of the cell. The mean effective conductance of ChR1-(1–345) was 0.054 ± 0.009 μS/pF ($n = 20$), whereas that of ChR2-(1–315) was 0.228 ± 0.037 μS/pF ($n = 20$) with a significant difference ($p < 0.0001$). The conductance was one of the differences between ChR1-(1–345) and ChR2-(1–315) photocurrent as noted previously (16). Its difference would result partly from the difference of expres-

sion in the plasma membrane (Fig. 2*B*). When the extracellular Na^+ was reduced from 142 to 20 mM, the reversal potential (E_{rev}) of the ChR1-(1–345) peak photocurrent was shifted from 12.6 ± 2.5 to -24.9 ± 2.3 mV (Fig. 3*E*), whereas that of ChR2-(1–315) was shifted from 13.9 ± 1.8 to -21.1 ± 2.0 mV (Fig. 3*F*). As a result the Na^+-dependent shift of E_{rev}, $\Delta E_{rev}(Na^+)$, of ChR1-(1–345) was -37.5 ± 2.2 mV ($n = 11$), which was similar to that of ChR2-(1–315) (-35.0 ± 1.1 mV, $n = 11$), and the difference was insignificant. Similar results were obtained when the plateau photocurrents were compared. Therefore, we concluded that ChR1-(1–345) and ChR2-(1–315) are similar in terms of the relative Na^+ permeability to other cations (K^+, H^+, Ca^{2+}, Mg^{2+}, and N-methyl-D-glucamine$^+$) at pH 7.4. At pH 6.0, as noted previously (10), the ChR1 photocurrent was large in effective conductance with very positive E_{rev} and showed little dependence on Na^+ (supplemental data 5) as the relative Na^+ permeability of ChR1 is dependent on the pH and is small at low pH (13).

Wavelength-Photocurrent Relationships of the Chimera Channelrhodopsins—The wavelength sensitivity of the photocurrent was similarly investigated for each chimera channelrhodopsin expressed in HEK293 cells. As shown in Fig. 4*A*, each wavelength relationship of the chimera photocurrent was intermediate between ChR1-(1–345) and ChR2-(1–315). For example, in the case of ChR(ABCDEfg), the light sensitivity was maximal at 480 nm, but the photocurrent was more preferably activated at wavelengths 500–540 nm than the wild-type ChR2. The wavelength sensitivity was well quantified by the ratio of the mean photocurrent at 500 and 520 nm to the mean at 440 and 460 nm (G/B ratio) (Fig. 4*B*). Although the significant enhancement of G/B ratio was limited to the exchange of segment "e" of ChR2-(1–315) with "E" ("e"-to-"E" exchange) or "g"-to-"G" exchange, it was significantly greater than that of ChR2-(1–315) but significantly smaller than that of ChR1-(1–345) in chimeras ChR(ABcdefg), ChR(ABCdefg), ChR(ABCDEfg), and ChR(ABCDEFg) ($p < 0.005$).

Ion Permeability of Chimera Channelrhodopsins—The ion permeability was again investigated for each chimera channelrhodopsin by comparing the *I-V* relationships at high Na^+ (142 mM) and low Na^+ (20 mM) extracellular environments (Fig. 5*A*). As summarized in Fig. 5*B*, the $\Delta E_{rev}(Na^+)$ was similar to those of ChR1-(1–345) and ChR2-(1–315) in the cases of ChR(ABcdefg), ChR(ABCdefg), ChR(ABCDefg), ChR(ABCDEfg), and ChR(ABCDEFg). Therefore, these chimera channelrhodopsins are similar to ChR2-(1–315) in terms of the relative Na^+ permeability to other cations (K^+, H^+, Ca^{2+}, Mg^{2+}, and N-methyl-D-glucamine$^+$) at pH 7.4. However, the absolute $\Delta E_{rev}(Na^+)$ of ChR(Abcdefg) was significantly smaller than those of the others. It is possible that the permeability of this chimera is less selective to Na^+ and permeable to large cations such as N-methyl-D-glucamine$^+$ (11).

The photocurrents of ChR(Abcdefg) and other chimera channelrhodopsins were also less rectified than that of ChR2-(1–315) in their *I-V* relationships (Fig. 5*A*; supplemental data 4). On the other hand as shown in Fig. 5*C*, the effective conductance was variable among chimera channelrhodopsins. It was significantly enhanced by the "b"-to-"B" or "e"-to-"E" exchange, whereas significantly reduced by the "d"-to-"D" or
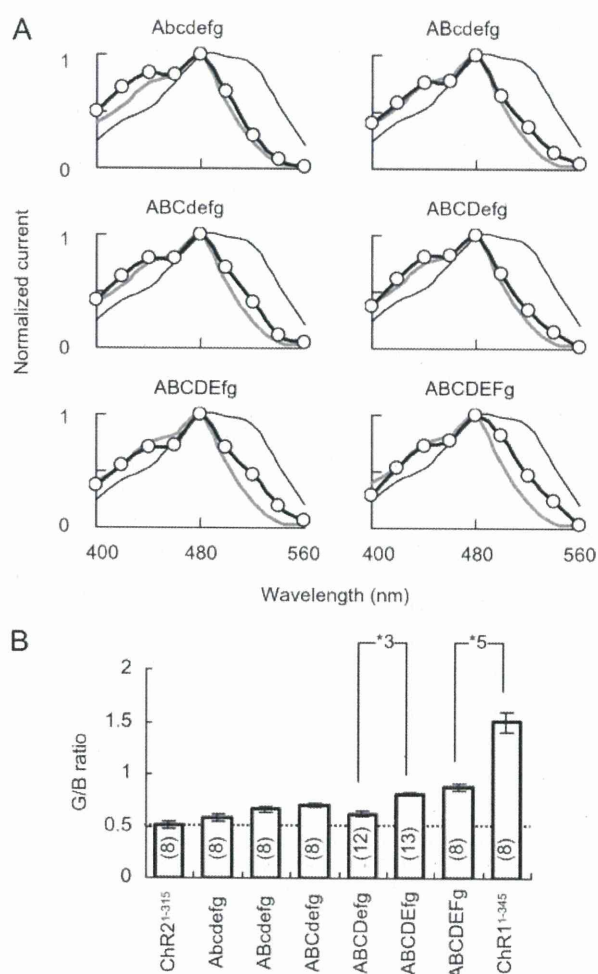

FIGURE 4. **Wavelength sensitivities of chimera photocurrents.** *A*, wavelength-photocurrent relationship of each chimera (*open circles*) is shown in comparison with those of ChR1-(1–345) (*black thin line*) and ChR2-(1–315) (*gray thick line*); ChR(*Abcdefg*), ChR(*ABcdefg*), ChR(*ABCdefg*), ChR(*ABCDefg*), ChR(*ABCDEfg*), and ChR(*ABCDEFg*). *B*, summary of G/B ratio of photocurrents (mean $\pm$ S.E.).

"f"-to-"F" exchange. The effective conductance is dependent on the single channel conductance, the probability of a channel being open and the channel density in the plasma membrane. The results of Fig. 5*C* were consistent with the high fluorescence density at the plasma membrane (Fig. 2*B*) in the cases of ChR(ABcdefg), ChR(ABCdefg), and ChR(ABCDEfg). Therefore, the large effective conductance was partly attributable to the high channel density, although there remains a possibility that other factors are different. Because the effective conductance was smaller than expected from the fluorescence density in the cases of ChR(ABCDefg) and ChR(ABCDEFg), either the single channel conductance or the probability of a channel being open was possibly small in these cases.

Photocurrent Profiles of Chimera Channelrhodopsins—When an LED light was applied as a square pulse, the ChR2-(1–315) photocurrent peaked almost instantaneously, desensitized rapidly to a steady state within 1 s, and turned off rapidly. Because the photocurrent kinetics are dependent on the light intensity, the holding potential as well as pH, the photocurrents of chimera channelrhodopsins were measured at the maximal
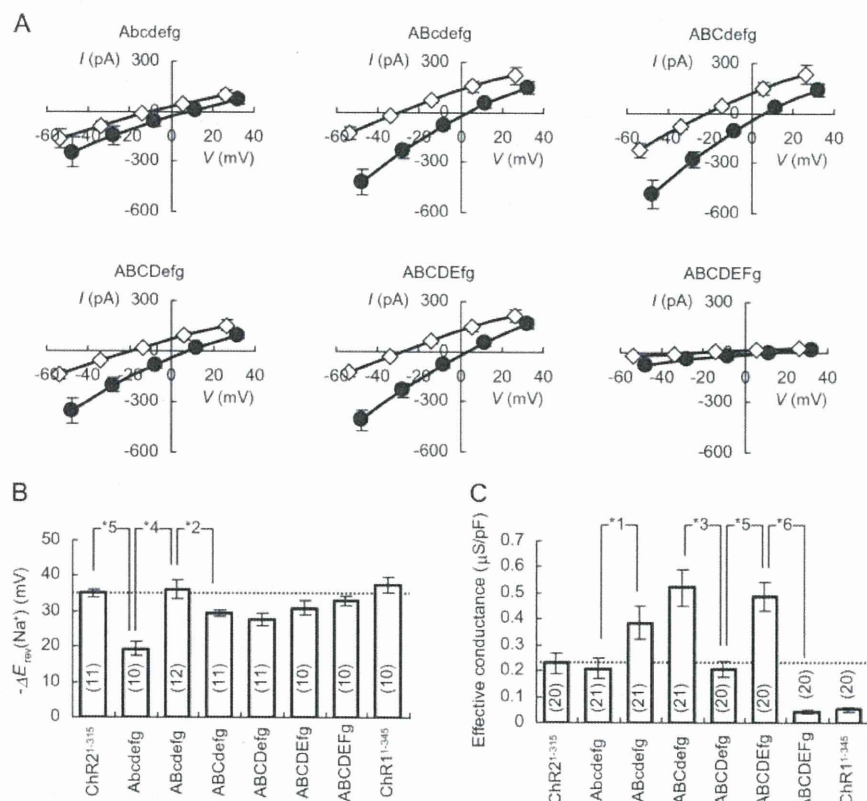
A

B

C

FIGURE 5. **Ion permeability of chimera.** *A*, *I-V* relationship of each chimera (mean ± S.E.). The currents were recorded under environments containing 120 mM $[Na^+]_i$ and 142 mM $[Na^+]_o$ (*filled circles*) or 20 mM $[Na^+]_o$ (*open diamonds*). *B*, summary (mean ± S.E.) of the Na^+-dependent reversal potential shift of each chimera between 142 and 20 mM $[Na^+]_o$, $\Delta E_{rev}(Na^+)$. *C*, summary (mean ± S.E.) of the effective conductance of each chimera.
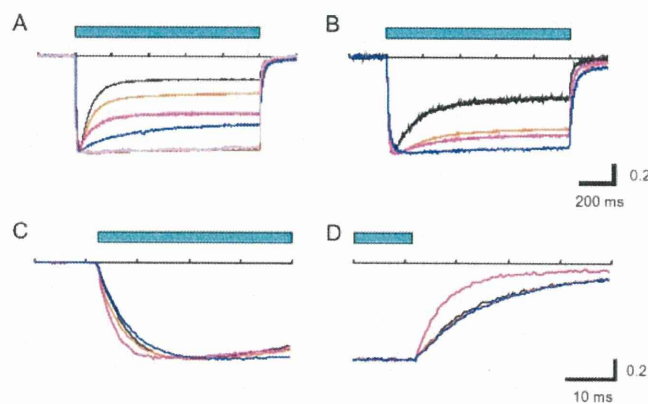
A

B

C

D

FIGURE 6. **Photocurrent profiles.** *A*, normalized photocurrent profiles of ChR2-(1–315) (*black*), ChR(Abcdefg) (*orange*), ChR(ABcdefg) (*magenta*), ChR(ABCDEfg) (*blue*), ChR(ABCDEFg) (*purple*), and ChR1-(1–345) (*brown*) in response to 1-s blue LED illumination at the maximal power density (0.077 mW mm^{-2}). *B*, normalized profiles of integrated photocurrents at wavelengths 400–560 nm. *C*, ON phase of photocurrents normalized to its peak; ChR2-(1–315) (*black*), ChR(Abcdefg) (*orange*), ChR(ABcdefg) (*magenta*), and ChR(ABCDEfg) (*blue*). *D*, OFF phase of the photocurrents normalized to those at the end of illumination; ChR2-(1–315) (*black*), ChR(Abcdefg) (*orange*), ChR(ABcdefg) (*magenta*), and ChR(ABCDEfg) (*blue*).

LED power, at the holding potential of −20 mV and at pH 7.2 inside and pH 7.4 outside of membrane. Although the photocurrents of ChR(Abcdefg), ChR(ABcdefg), ChR(ABCdefg), and ChR(ABCDEfg) showed characteristic peak-and-plateau

time courses like ChR2-(1–315), they were found to be diverse in their kinetics (Fig. 6*A*). The desensitization of the ChR(Abcdefg) photocurrent was smaller than that of ChR2-(1–315) but larger than that of ChR(ABcdefg) with the maximal LED power. With the progressing replacement of N-terminal segments, the desensitization had a tendency to be further reduced, *e.g.* ChR(ABCDEfg). The magnitude of desensitization was normalized by the peak current and compared among the channelrhodopsins (Fig. 7*A*). The desensitization was significantly reduced by the "a"-to-"A" exchange and was further by "b"-to-"B" exchange. Although the contributions to the desensitization of segments "C/c" and "D/d" were small, "e"-to-"E" exchange significantly reduced the desensitization. The "f"-to-"F" exchange further reduced the desensitization, but to a significantly larger level than that of ChR1. The reduced desensitization of ChR(ABCDEfg), ChR(ABCDEFg), and ChR1-(1–345) may come from the shift of the sensitivity-wavelength relationship. To test this, using the data of Fig. 4*A*, the photocurrents measured at each wavelength from 400 to 560 nm are integrated (Fig. 6*B*), and the desensitization was evaluated on this integrated photocurrent. As shown in Fig. 7*B*, the desensitization of the integrated photocurrent was well correlated to that evoked by the maximal LED power ($r = 0.96$, $p < 0.0005$, paired t test). Therefore, the reduced desensitization cannot be explained by the shift of the sensitivity-wavelength relationship. However, the difference between ChR(ABCDEFg) and ChR1-(1–345) in Fig. 7*A* may be attributed to the different wavelength sensitivity because no obvious difference was observed in the desensitization of the integrated photocurrents (Fig. 7*B*).

These photocurrents were also variable in their turning-on (ON) and turning-off (OFF) kinetics. As shown in Fig. 6, *C* and *D*, where the LED light pulse was applied at its maximal power, the photocurrent of ChR(Abcdefg) was faster than that of ChR2-(1–315) in the ON kinetics, whereas the two were similar in the OFF kinetics. The photocurrent of ChR(ABcdefg) was faster than that of ChR(Abcdefg) in both ON and OFF, whereas that of ChR(ABCDEfg) was similar to ChR2-(1–315) in both ON and OFF. The ON time constant (τ_{ON}) of ChR2 is a function of the LED power, whereas the effective OFF time constant (τ_{OFF}) is not (14). Therefore, the τ_{ON} and τ_{OFF} were both compared at the maximum LED power (Fig. 7, *C* and *D*). The contribution of segment "A/a" to the τ_{OFF} was negligible, whereas both the τ_{OFF} and τ_{ON} became significantly small by replacing
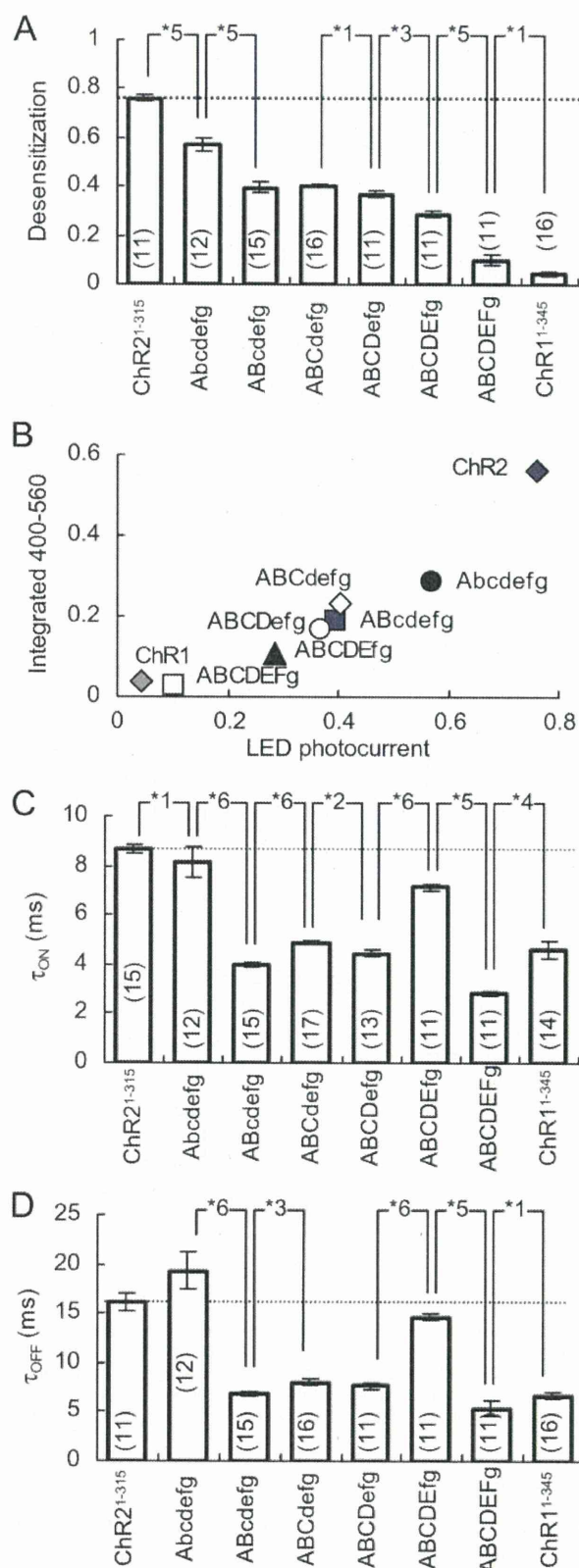
FIGURE 7. **Desensitization, ON, and OFF kinetics.** A, magnitude of desensitization was normalized by the peak photocurrent and summarized for channelrhodopsins (mean ± S.E.). B, correlation of desensitization between the integrated photocurrent and the LED-evoked photocurrent. C, summary of ON time constants (τ_{ON}, mean ± S.E.). D, summary of effective OFF time constants (τ_{OFF}, mean ± S.E.).
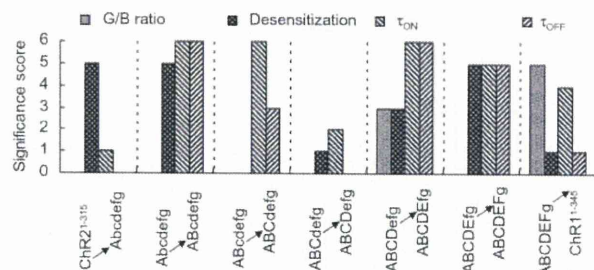

FIGURE 8. **Effects of segment substitution.** The significance scores were compared for four photocurrent properties, the G/B ratio, desensitization, τ_{ON}, and τ_{OFF} among the segment substitutions (from *left* to *right*) as follows: ChR2-(1–315) *versus* ChR(Abcdefg), ChR(Abcdefg) *versus* ChR(ABcdefg), ChR(ABcdefg) *versus* ChR(ABCdefg), ChR(ABCdefg) *versus* ChR(ABCDefg), ChR(ABCDefg) *versus* ChR(ABCDEfg), ChR(ABCDEfg) *versus* ChR(ABCDEFg), and ChR(ABCDEFg) *versus* ChR1-(1–345).

segment "b" of ChR(Abcdefg) with "B." Although both the τ_{OFF} and τ_{ON} were significantly enlarged by "e"-to-"E" exchange, they were significantly reduced by "f"-to-"F" exchange.

Significance of E-segment as a Determinant of the Photocurrent Properties—The above results indicate that each photocurrent property was variably dependent on the segment exchanges. As shown in Fig. 8, the significance score of the Mann-Whitney U test was compared with the photocurrent properties of the G/B ratio, desensitization, and τ_{ON} and τ_{OFF}, and the effects of each single segment exchange were evaluated as follows: from ChR2-(1–315) to ChR(Abcdefg), from ChR(Abcdefg) to ChR(ABcdefg), from ChR(ABcdefg) to ChR(ABCdefg), from ChR(ABCdefg) to ChR(ABCDefg), from ChR(ABCDefg) to ChR(ABCDEfg), from ChR(ABCDEfg) to ChR(ABCDEFg), or from ChR(ABCDEFg) to ChR1-(1–345). Because the "b"-to-"B" and "f"-to-"F" exchanges definitely affected the photocurrent kinetics as well as the effective conductance, these structures may be related to the channel properties. On the other hand, the "g"-to-"G" exchange more definitely influenced the G/B ratio than photocurrent kinetics. We found that all four properties were definitely affected by the "e"-to-"E" exchange. Therefore, it is suggested that segment "E/e" is one of the key determinants of photocurrent properties such as the wavelength sensitivity and the kinetics.

To further test whether the segment "E/e" is sufficient to determine the photocurrent properties, the effect of a single segment exchange from "e" to "E" was investigated. The $\Delta E_{rev}(Na^+)$ of ChR(abcdEfg) was -36.6 ± 3.1 mV ($n = 11$), which was the same as that of ChR2-(1–315) (-35.0 ± 3.5 mV, $n = 11$). The effective conductance of ChR(abcdEfg) was 0.173 ± 0.053 μS/pF ($n = 20$), which was not significantly different from that of ChR2-(1–315). Similar to the case of ChR(ABCDEfg), the light sensitivity was maximal at 480 nm, but there was a preference to 500–540 nm in the case of ChR(abcdEfg). The G/B ratio of ChR(abcdEfg) was 0.85 ± 0.05 ($n = 8$), which was similar to that of ChR(ABCDEfg) but significantly larger than that of ChR2-(1–315) (Fig. 9). The segments "e" and "E" are different only at eight amino acid residues (Fig. 1A). To identify the residues involved in the wavelength preference, we replaced one-by-one each amino acid residue in "e" with the corresponding one of "E" yielding eight channel-
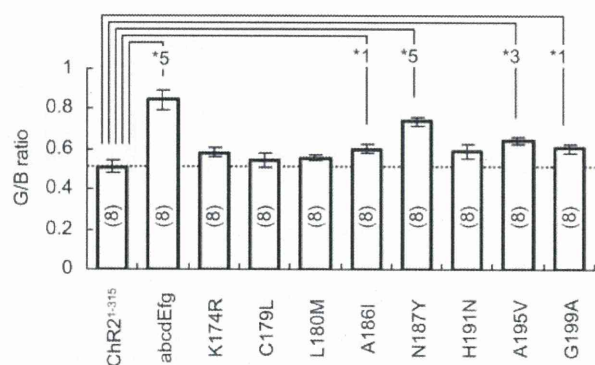
FIGURE 9. **Wavelength sensitivities of E-segment substitutions.** Summary of G/B ratios of photocurrents (mean ± S.E.). The *number with an asterisk* indicates the significance score to ChR2-(1–315) (Mann-Whitney *U* test).

rhodopsins as follows: ChR2(K174R), ChR2(C179L), ChR2-(L180M), ChR2(A186I), ChR2(N187Y), ChR2(H191N), ChR2-(A195V), and ChR2(G199A). The G/B ratio of each amino acid replacement of ChR2-(1–315) is summarized in Fig. 9. The G/B ratio of ChR2(N187Y) was as large as that of ChR(abcdEfg). A small but significantly large G/B ratio was also observed in ChR2(A186I), ChR2(A195V), and ChR2(G199A).

The photocurrent profile of ChR(abcdEfg) was obviously different from those of ChR2-(1–315) (Fig. 10*A*). As summarized in Fig. 10, *B* and *D*, the ChR(abcdEfg) photocurrent was small in the desensitization but large in both the τ_{ON} and τ_{OFF}. The one-by-one amino acid exchanges from "e" to "E" variably changed the photocurrent profile. For example, the desensitization was strongly reduced in ChR2(N187Y) and ChR2(H191N) (Fig. 10*B*). The τ_{ON} was enlarged in ChR2(C179L), ChR2(N187Y), and ChR2(G199A) but reduced in ChR2(L180M) and ChR2(A186I) (Fig. 10*C*). The τ_{OFF} was strongly enlarged in ChR2(N187Y) but reduced in ChR2(L180M) and ChR2(A186I) (Fig. 10*D*).

To evaluate the effects of the amino acid exchanges, the statistical significance was scored according to the *p* value of the Mann-Whitney *U* test as done previously. Fig. 11*A* summarizes the significance scores of the single segment and the single amino acid exchanges from "e" to "E." We found that all four photocurrent properties, the G/B ratio, desensitization, τ_{ON}, and τ_{OFF}, were definitely affected by the single segment exchange from ChR2-(1–315) to ChR(abcdEfg). These properties were also definitely changed in ChR2(N187Y). The ChR2(N187Y) resembled ChR(abcdEfg) in all four properties.

The above results suggest that the position Tyr[226]("E")/Asn[187]("e") is one of the possible determinants of the wavelength dependence of the photocurrent. To test this, we examined the wavelength sensitivity of a targeted mutant of ChR1-(1–345), ChR1(Y226N), in which Tyr[226] of ChR1-(1–345) was replaced with Asn. As shown in Fig. 12*A*, this mutation blue-shifted the wavelength-photocurrent relationship toward that of ChR2-(1–315). The G/B ratio of ChR1(Y226N) was 0.97 ± 0.06 (*n* = 8), which was significantly smaller than that of ChR1-(1–345) (Fig. 12*B*). The ChR1(Y226N) was also different from ChR1-(1–345) in the photocurrent kinetics (Fig. 12*C*), the enhancement of desensitization (Fig. 12*D*), the elongation of τ_{ON} (Fig. 12*E*), and the reduction of τ_{OFF} (Fig. 12*F*).
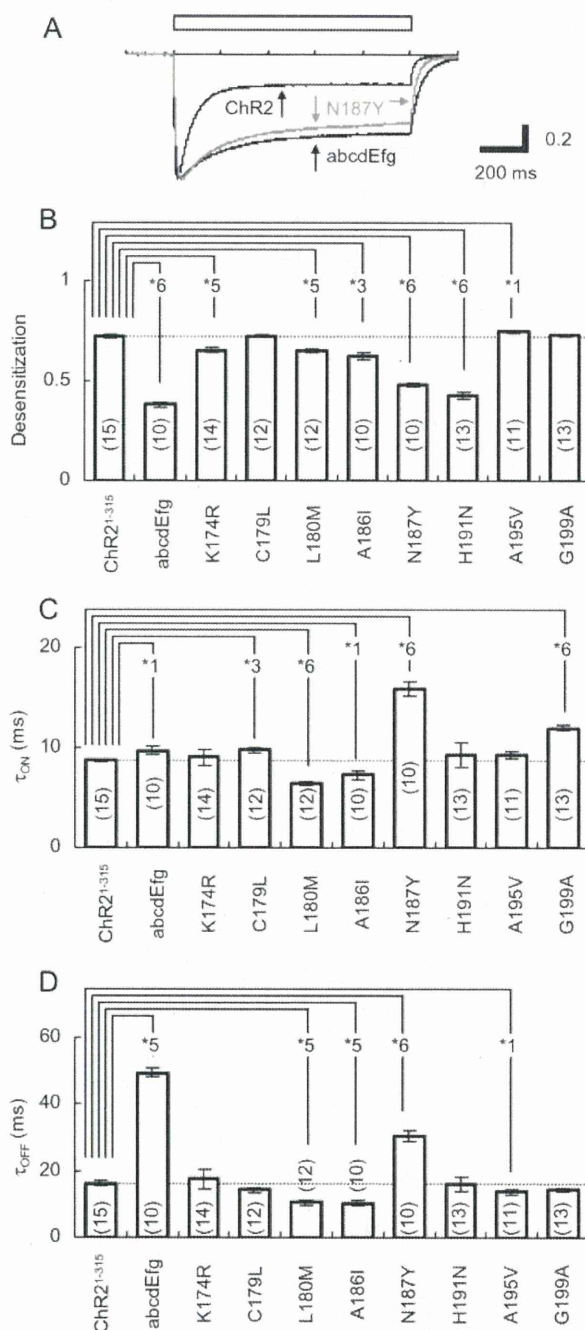

FIGURE 10. **Photocurrent kinetics of E-segment substitutions.** *A*, normalized photocurrent profiles of ChR2-(1–315) (*black line*), ChR(abcdEfg) (*black line*), and ChR2(N187Y) (*gray line*) in response to 1-s blue LED illumination at the maximal power. *B*, summary of photocurrent desensitization (mean ± S.E.). *C*, summary of τ_{ON} (mean ± S.E.). *D*, summary of τ_{OFF} (mean ± S.E.).

DISCUSSION

Molecular Determinants Differentiating ChR2 from ChR1— In this study we divided ChR2-(1–315) into seven segments, "a" to "g," so that each segment contained one of the seven putative transmembrane domains. By replacing the N-terminal segments of ChR2-(1–315) with the homologous counterparts of ChR1-(1–345), "A" to "F," we identified the structure differentiating ChR2 from ChR1. The G/B ratio of the photocurrent,
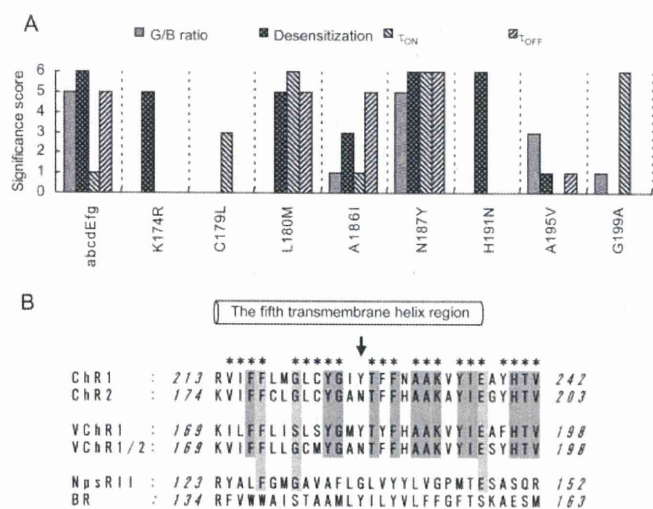
FIGURE 11. **Effects of E-segment substitutions.** *A,* significance scores were compared for four photocurrent properties, the G/B ratio, desensitization, τ_{ON}, and τ_{OFF} among E-segment substitutions. *B,* alignment of the fifth transmembrane domain sequences from ChR1, ChR2, and their phylogenic relatives: channelrhodopsins from *V. carteri* (VChR1 and VChR1/2), sensory rhodopsin II from *N. pharaonis* (NpsRII), and bacteriorhodopsin from *H. salinarum* (BR). The putative fifth transmembrane domain is indicated by the *cylinder*. The identical amino acids between ChR1 and ChR2 are indicated with an *asterisk. Gray background,* the amino acid residues conserved among four channelrhodopsins, ChR1, ChR2, VChR1, and VChR1/2. *Ash background,* the amino acid residues conserved among ChR1, ChR2, and NpsRII. The *arrow* indicates Tyr[226](ChR1)/Asn[187](ChR2) position.

FIGURE 12. **Photocurrent properties of ChR1(Y226N).** *A,* wavelength relationship of ChR1(Y226N) (*open circles*) is shown in comparison with those of ChR1-(1–345) (*black thin line*) and ChR2-(1–315) (*gray thick line*) photocurrents. *B,* summary of the effect of Y226N exchange on the G/B ratio. *C,* normalized photocurrent profiles of ChR1-(1–345) (*gray*) and ChR1(Y226N) (*black*) in response to 1-s blue LED illumination at the maximal power density (0.077 mW mm⁻²). The time scale is 200 ms/division. The effect of Y226N exchange was summarized on the desensitization (*D*), τ_{ON} (*E*), and τ_{OFF} (*F*) of photocurrents (mean ± S.E.).

used to evaluate the wavelength preference, was gradually increased with the replacements of the N-terminal segments, "A/a" to "C/c," and further by the "e"-to-"E" replacement. But the effect of the "g"-to-"G" replacement was the most definitive, suggesting that the seventh transmembrane helix has structures involved in the color tuning of the molecule. Previously, ChR1 and ChR2 have been differentiated in the relative permeability of Na⁺ (10, 11). However, as the cation selectivity of ChR1 photocurrent is dependent on the pH, the photocurrent is less dependent on Na⁺ at low pH (13). Consistent with this notion, we did not find any difference in the ion selectivity at pH 7.4. On the other hand, they were differentiated by the effective conductance as noted previously (16). The effective conductance was large even when the first five segments "a" to "e" of ChR2-(1–315) were replaced by "A" to "E" of ChR1-(1–345). The large effective conductance of this chimera channelrhodopsin was in part attributable to the expression level in the plasma membrane. However, further "f"-to-"F" replacement reduced the effective conductance to as small as that of ChR1-(1–345). This is somewhat inconsistent with the fluorescence density of these molecules in the plasma membrane. The "F/f" segment itself or its interaction with other segments is likely to be involved in the regulation of channel conductance or probability of a channel being open. We profiled the photocurrent kinetics by three quantities, the desensitization, τ_{ON}, and τ_{OFF}. Although variable, the chimeras ChR(Abcdefg), ChR(ABcdefg), ChR(ABCdefg), ChR(ABCDefg), and ChR(ABCDEfg) generated photocurrents with properties kinetically intermediate between ChR1-(1–345) and ChR2-(1–315). On the other hand, the chimera ChR(ABCDEFg) was kinetically more similar to
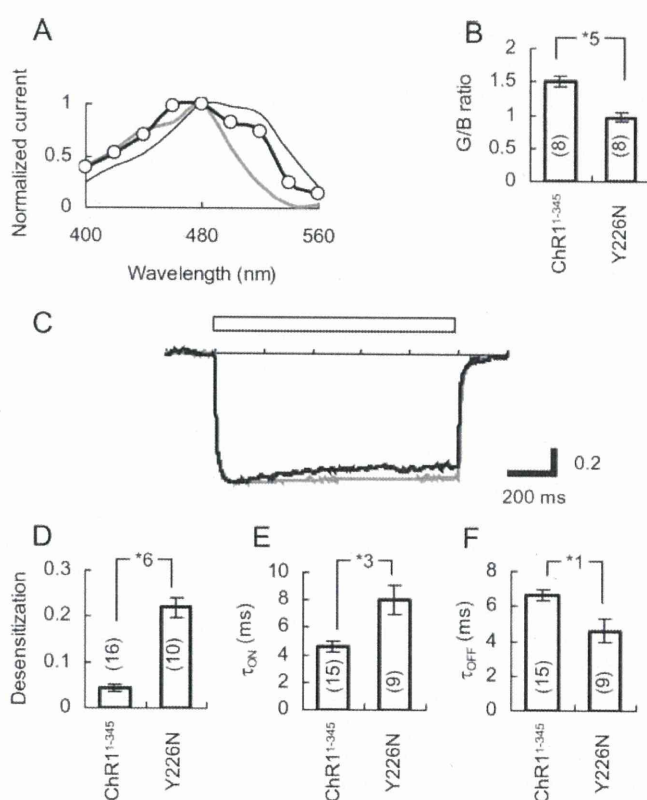
ChR1-(1–345). Taken together, the properties differentiating the photocurrent kinetics of ChR1 from those of ChR2 are not confined to a specific structure, but are variably influenced by the exchange of each segment. Even the exchanges of the "C/c" and "D/d" segments definitely changed the photocurrent properties, although the third and the fourth transmembrane domains are highly conserved among channelrhodopsins (16, 17). This is consistent with the notion that these domains are also involved in the channel properties of ChR2-(1–315), and indeed, the single amino acid mutation H134R enhanced the photocurrent amplitude (19). In this study we further investigated the "E/e" segment because it definitely changed the photocurrent properties without reducing the effective conductance.

Fifth Transmembrane Helix as the Determinant of Wavelength Sensitivity—In relation to other archaea-type rhodopsins, interactions between the retinal chromophore and its protein environment are the determinants of the wavelength preferences. Three factors are suggested to be involved in these interactions (20, 21) as follows: (i) the strength of the protein environment forcing the retinal to be a coplanar 6s-trans conformation; (ii) the protein environment electrically interacting with the chromophore with its counter ion or hydrogen bond acceptor; and (iii) a less well defined long range coupling, which

is thought to involve the interaction of polar or polarizable amino acid groups with the chromophore, influencing the stability of the ground state. The amino acid residues assumed to be related to these interactions are mostly present from the third to the seventh transmembrane domains (22, 23) and are almost conserved between ChR1 and ChR2 (Fig. 1), *e.g.* the consensus retinal-binding residue, Lys[296]("G" segment)/Lys[257]("g" segment) in the seventh transmembrane domain; the consensus residues defining the Schiff base counterion complex, Arg[159]("B")/Arg[120]("b") and Glu[162]("B")/Glu[123]("b") in the third transmembrane domain; and Asp[292]("G")/Asp[253]("g") in the seventh transmembrane domain, which are critical for the wavelength preference (17, 24, 25). The nonpolar amino acid residues involved in the retinal-Schiff base binding pocket, Gly[220]("E")/Gly[181]("e"), Leu[221]("E")/Leu[182]("e"), and Cys[222]("E")/Cys[183]("e") in the fifth transmembrane domain, which are predicted to be closely located to the β-ionone ring of retinal, are all conserved between ChR1 and ChR2 (17). Other amino acid residues that affect the electron distribution of the retinal-Schiff base are Asn[153]("B")/His[114]("b"), Glu[274]("F")/Glu[235]("f"), and Ser[284]("G")/Ser[245]("g"). However, the wavelength sensitivity of the chimera was only minimally changed by the "b"-to-"B" exchange. On the other hand, the single "e"-to-"E" exchange of ChR2-(1–315) red-shifted the wavelength sensitivity of the photocurrent, and the single "E"-to-"e" exchange of ChR(ABCDEfg) blue-shifted it. This indicates the presence of another structure either regulating the electron distribution of the retinal-Schiff base or interacting with it through long range coupling. The results of our experiments using ChR2(N187Y) and ChR1(Y226N) indicate that one-by-one amino acid replacement of Asn[187]("e") to the corresponding Tyr red-shifted the sensitivity-wavelength relationship, whereas the reverse replacement of Tyr[226]("E") to Asn blue-shifted it. The position of Tyr[226]("E")/Asn[187]("e") would lie adjacent to the nonpolar retinal binding pocket if the α-helix structure is predicted for the fifth transmembrane domain. It is possible that these amino acid residues have some additional interaction with retinal. The hydroxyl-bearing Tyr[226] would probably interact preferentially with the excited-state charge distribution around the β-ionone ring of retinal to lower the excitation energy and red-shift the absorption spectrum (26, 27). Alternatively, these residues may interact with retinal-Schiff base with long range coupling.

An alignment of the motif corresponding to the fifth transmembrane helix domain for ChR1 and ChR2 is shown in Fig. 11*B*, in comparison with the other phylogenic relatives. The recently identified channelrhodopsins from *Volvox carteri*, VChR1 (17) and VChR1/2 (28), are highly homologous to both ChR1 and ChR2. Of 18 amino acids conserved between ChR1 and ChR2, 12 are found in both VChR1 and VChR1/2, 4 are found only in VChR1/2, and 1 is found only in VChR1. The counterpart of Tyr[226](ChR1)/Asn[187](ChR2) is Asn in the case of blue-absorbing VChR1/2, whereas it is Tyr in the case of more red-shifted VChR1. Although this is consistent with the present result that Asn-to-Tyr replacement red-shifted the absorption spectrum, the involvement of other amino acid residues should not be excluded. On the other hand, the sequences of sensory rhodopsin II from *Natronobacterium*

pharaonis (the maximum absorption at 500 nm) and bacteriorhodopsin from *Halobacterium salinarum* (the maximum absorption at 550 nm) are less homologous in this region. Of 18 amino acids conserved between ChR1 and ChR2, 3 are found only in sensory rhodopsin II and 0 in bacteriorhodopsin. It is thus possible that the color-tuning contribution of the fifth transmembrane domain is different in these prokaryotic rhodopsins.

Fifth Transmembrane Helix as the Determinant of Photocurrent Kinetics—The "E/e" segment, which contains the fifth transmembrane helix, was also one of the structural determinants of the photocurrent kinetics. When the "e"-to-"E" exchange was made on chimera ChR(ABCDefg), the desensitization was reduced, whereas both the τ_{ON} and τ_{OFF} were definitely enlarged. It was also the case when the same exchange was made on ChR2-(1–315). Therefore, the photocurrent kinetics such as desensitization, τ_{ON}, and τ_{OFF} are dependent on the structure intrinsic to the "E/e" segment. In the "E/e" segment the amino acid residue Tyr[226]("E")/Asn[187]("e") again was central in determining the photocurrent kinetics. The desensitization was strongly reduced in ChR2(N187Y) and ChR2(H191N), whereas it was enhanced by Y226N exchange of ChR1-(1–345). However, it was also dependent on other structural components such as the "A/a" and "B/b" segments. The τ_{OFF} was definitely enhanced in ChR2(N187Y) but reduced in ChR2(L180M) and ChR2(A186I). The Y226N exchange of ChR1-(1–345) also reduced τ_{OFF}. It is thus suggested that the position Tyr[226]("E")/Asn[187]("e") is involved in the channel closure but that the interaction with other key residues is important. However, both the N187Y exchange of ChR2-(1–315) and the Y226N exchange of ChR1-(1–345) elongated τ_{ON}. Because τ_{ON} is dependent on the light intensity (14) but is also expected to be dependent on τ_{OFF} as a consequence of the photocycle response (18, 28, 29), further studies are necessary to reveal the variability of this value.

Conclusion—This work revealed the significance of the fifth transmembrane helix, particularly its residue Tyr[226](ChR1)/Asn[187](ChR2), as a molecular determinant differentiating the photocurrent properties between ChR1 and ChR2. Chimeric mutation by a segment exchange has been a powerful tool for identifying the molecular determinants involved in a certain function. For the first time, this study made a series of chimeric mutations by replacing the molecular segments containing each transmembrane helix of ChR2 with the homologous counterparts of ChR1. Based on systematic and quantitative studies of the distribution of the molecules, wavelength sensitivity, reversal potential, and kinetic profile, it is suggested that the fifth transmembrane helix is involved in both the wavelength sensitivity and the kinetic profile of the photocurrent. Moreover, all these results strongly suggest that the residue Tyr[226]("E")/Asn[187]("e") lies at a key position enabling it to interact with the retinal-Schiff base. It also lies at a position interacting with other residues involved in the photocurrent kinetic profiles such as desensitization, τ_{ON}, and τ_{OFF}. The significance of Tyr[226]("E")/Asn[187]("e") has to be further investigated by mutations replacing Asn[187] of ChR2-(1–315) with various amino acid residues and/or by x-ray crystallographic analysis (20, 30).

Recently the ChR2-mediated photostimulation of neurons has been applied to investigate the function of neural networks *in vivo* (31–34). Moreover, ChR2-expressing transgenic animals have been generated that are successfully used to study the neural basis of behavioral responses in *Caenorhabditis elegans* (19), zebrafish (35), and mammals (36). Given its superiority in spatio-temporal resolution, ChR2 has become a powerful tool for the investigation of neural networks.

ChR2 is also a potential tool as a visual prosthesis for photoreceptor degeneration (37). In retinal degenerative diseases such as retinitis pigmentosa, photoreceptor cells are lost while preserving the inner retinal neurons such as retinal ganglion cells and bipolar cells. Exogenous expression of ChR2 in these neurons using viral vectors (38, 39) or *in vivo* electroporation methods (40) restores visually evoked responses in the visual cortex of rodents.

However, some further technological developments are necessary to achieve the full potential of ChR2. First, photosensitive channels with various wavelength sensitivities are desirable. One of the *Volvox*-derived channelrhodopsins, VChR1, may be a candidate because it has a peak absorbance at 540 nm (17). Second, the small single channel conductance of ChR2 (in the magnitude of fS) (12, 37) should be compensated by facilitating the membrane expression. Alternatively, it would be useful to develop a ChR2 with increased single channel conductance. Third, the prominent desensitization of ChR2 photocurrent limits its application for repetitive stimulation at high frequency. This could be overcome by reducing the desensitization or facilitating the recovery rate.

Some of the chimera channelrhodopsins have several advantages over the wild-type ChR2 in applying to the light-induced membrane depolarization (14, 31, 41). For example, the chimera ChR(ABCDEfg) is sensitive to wavelengths of 480–540 nm, has large effective conductance when expressed in HEK293 cells, and its photocurrent desensitization was almost negligible. Moreover, its ON and OFF kinetics were the same as those of ChR2. Therefore, this chimera, to which we give the name "channelrhodopsin/wide receiver," would become a good tool to stimulate neurons repetitively with low intensity flash light and also a potential tool as a visual prosthesis of photoreceptor degeneration (38, 39). Another potentially useful chimera is ChR(ABcdefg) because it is very fast in both its ON and OFF kinetics. It is also characterized by small desensitization and large effective conductance. This chimera, to which we give the name "channelrhodopsin/fast receiver," would become a good tool to stimulate neurons repetitively at high frequency flash. The application of channelrhodopsins would be facilitated by this new lineup of chimeras.

REFERENCES

1. Nathans, J., Thomas, D., and Hogness, D. S. (1986) *Science* **232,** 193–202
2. Nathans, J. (1999) *Neuron* **24,** 299–312
3. Palczewski, K. (2006) *Annu. Rev. Biochem.* **75,** 743–767
4. Kaupp, U. B., and Seifert, R. (2002) *Physiol. Rev.* **82,** 769–824
5. Bradley, J., Reisert, J., and Frings, S. (2005) *Curr. Opin. Neurobiol.* **15,** 343–349
6. Melkonian, M., and Robenek, H. (1980) *J. Ultrastruct. Res.* **72,** 90–102
7. Sineshchekov, O. A., Jung, K.-H., and Spudich, J. L. (2002) *Proc. Natl. Acad. Sci. U. S. A.* **99,** 8689–8694
8. Suzuki, T., Yamasaki, K., Fujita, S., Oda, K., Iseki, M., Yoshida, K., Watanabe, M., Daiyasu, H., Toh, H., Asamizu, E., Tabata, S., Miura, K., Fukuzawa, H., Nakamura, S., and Takahashi, T. (2003) *Biochem. Biophys. Res. Commun.* **301,** 711–717
9. Kateriya, S., Nagel, G., Bamberg, E., and Hegemann, P. (2004) *News Physiol. Sci.* **19,** 133–137
10. Nagel, G., Ollig, D., Fuhrmann, M., Kateriya, S., Musti, A. M., Bamberg, E., and Hegemann, P. (2002) *Science* **296,** 2395–2398
11. Nagel, G., Szellas, T., Huhn, W., Kateriya, S., Adeishvili, N., Berthold, P., Ollig, D., Hegemann, P., and Bamberg, E. (2003) *Proc. Natl. Acad. Sci. U. S. A.* **100,** 13940–13945
12. Hegemann, P. (2008) *Annu. Rev. Plant. Biol.* **59,** 167–189
13. Berthold, P., Tsunoda, S. P., Ernst, O. P., Mages, W., Gradmann, D., and Hegemann, P. (2008) *Plant Cell* **20,** 1665–1677
14. Ishizuka, T., Kakuda, M., Araki, R., and Yawo, H. (2006) *Neurosci. Res.* **54,** 85–94
15. Sambrook, J., and Russell, D. W. (2001) *Molecular Cloning: A Laboratory Manual,* 3rd Ed., pp. 13.36–13.39, Cold Spring Harbor Laboratory Press, Cold Spring Harbor, NY
16. Nagel, G., Szellas, T., Kateriya, S., Adeishvili, N., Hegemann, P., and Bamberg, E. (2005) *Biochem. Soc. Trans.* **33,** 863–866
17. Zhang, F., Prigge, M., Beyrière, F., Tsunoda, S. P., Mattis, J., Yizhar, O., Hegemann, P., and Deisseroth, K. (2008) *Nat. Neurosci.* **11,** 631–633
18. Hegemann, P., Ehlenbeck, S., and Gradmann, D. (2005) *Biophys. J.* **89,** 3911–3918
19. Nagel, G., Brauner, M., Liewald, J. F., Adeishvili, N., Bamberg, E., and Gottschalk, A. (2005) *Curr. Biol.* **15,** 2279–2284
20. Luecke, H., Schobert, B., Lanyi, J. K., Spudich, E. N., and Spudich, J. L. (2001) *Science* **293,** 1499–1503
21. Shimono, K., Hayashi, T., Ikeura, Y., Sudo, Y., Iwamoto, M., and Kamo, N. (2003) *J. Biol. Chem.* **278,** 23882–23889
22. Pebay-Peyroula, E., Royant, A., Landau, E. M., and Navarro, J. (2002) *Biochim. Biophys. Acta* **1565,** 196–205
23. Adamian, L., Ouyang, Z., Tseng, Y. Y., and Liang, J. (2006) *Photochem. Photobiol.* **82,** 1426–1435
24. Kloppmann, E., Becker, T., and Ullmann, M. (2005) *Proteins* **61,** 953–965
25. Hoffmann, M., Wanko, M., Strodel, P., König, P. H., Frauenheim, T., Schulten, K., Thiel, W., Tajkhorshid, E., and Elstner, M. (2006) *J. Am. Chem. Soc.* **128,** 10808–10818
26. Kochendoerfer, G. G., Lin, S. W., Sakmar, T. P., and Mathies, R. A. (1999) *Trends Biochem. Sci.* **24,** 300–305
27. Hillebrecht, J. R., Galan, J., Rangarajan, R., Ramos, L., McCleary, K., Ward, D. E., Stuart, J. A., and Birge, R. R. (2006) *Biochemistry* **45,** 1579–1590
28. Ernst, O. P., Sánchez Murcia, P. A., Daldrop, P., Tsunoda, S. P., Kateriya, S., and Hegemann, P. (2008) *J. Biol. Chem.* **283,** 1637–1643
29. Bamann, C., Kirsch, T., Nagel, G., and Bamberg, E. (2008) *J. Mol. Biol.* **375,** 686–694
30. Miyazawa, A., Fujiyoshi, Y., and Unwin, N. (2003) *Nature* **423,** 949–955
31. Li, X., Gutierrez, D. V., Hanson, M. G., Han, J., Mark, M. D., Chiel, H., Hegemann, P., Landmesser, L. T., and Herlitze, S. (2005) *Proc. Natl. Acad. Sci. U. S. A.* **102,** 17816–17821
32. Petreanu, L., Huber, D., Sobczyk, A., and Svoboda, K. (2007) *Nat. Neurosci.* **10,** 663–668
33. Huber, D., Petreanu, L., Ghitani, N., Ranade, S., Hromadka, T., Mainen, Z., and Svoboda, K. (2008) *Nature* **451,** 61–64
34. Kuhlman, S. J., and Huang, Z. J. (2008) *PLoS ONE* **3,** e2005

35. Douglass, A. D., Kraves, S., Deisseroth, K., Schier, A. F., and Engert, F. (2008) *Curr. Biol.* **18,** 1133–1137
36. Arenkiel, B. R., Peca, J., Davison, I. G., Feliciano, C., Deisseroth, K., Augustine, G. J., Ehlers, M. D., and Feng, G. (2007) *Neuron* **54,** 205–218
37. Herlitze, S., and Landmesser, L. T. (2007) *Curr. Opin. Neurobiol.* **17,** 87–94
38. Bi, A., Cui, J., Ma, Y. P., Olshevskaya, E., Pu, M., Dizhoor, A. M., and Pan, Z. H. (2006) *Neuron* **50,** 23–33
39. Tomita, H., Sugano, E., Yawo, H., Ishizuka, T., Isago, H., Narikawa, S., Kügler, S., and Tamai, M. (2007) *Investig. Ophthalmol. Vis. Sci.* **48,** 3821–3826
40. Lagali, P. S., Balya, D., Awatramani, G. B., Munch, T. A., Kim, D. S., Busskamp, V., Cepko, C. L., and Roska, B. (2008) *Nat. Neurosci.* **11,** 667–675
41. Boyden, E. S., Zhang, F., Bamberg, E., Nagel, G., and Deisseroth, K. (2005) *Nat. Neurosci.* **8,** 1263–1268

ORIGINAL PAPER

β-Phorbol ester-induced enhancement of exocytosis in large mossy fiber boutons of mouse hippocampus

Takuya Hikima · Rikita Araki · Toru Ishizuka ·
Hiromu Yawo

Abstract β-Phorbol esters (BPE), synthetic analogues of diacylglycerol (DAG), induce the potentiation of transmission in many kinds of synapses through activating the C_1 domain-containing receptors. However, their effects on synaptic vesicle exocytosis have not yet been investigated. Here, we evaluated the vesicular exocytosis directly from individual large mossy fiber boutons (LMFBs) in hippocampal slices from transgenic mice that selectively express synaptopHluorin (SpH). We found that the activity-dependent increment of SpH fluorescence (ΔSpH) was enhanced by 4β-phorbol 12,13-diacetate (PDAc), one of the BPEs, without influencing the recycled component of SpH. These PDAc effects on ΔSpH were almost completely inhibited by staurosporine, a non-selective antagonist of protein kinases. However, intermittent synaptic transmission was still potentiated through a staurosporine-resistant mechanism. The staurosporine-sensitive cascade may facilitate the vesicle replenishment, thus maintaining the fidelity of transmission at a high level during repetitive firing of the presynaptic neuron.

T. Hikima · R. Araki · T. Ishizuka · H. Yawo (✉)
Department of Developmental Biology and Neuroscience,
Tohoku University Graduate School of Life Sciences,
2-1 Seiryo-machi, Aoba-ku, Sendai 980-8575, Japan
e-mail: yawo@mail.tains.tohoku.ac.jp

T. Hikima · H. Yawo
Tohoku University Basic and Translational Research
Centre for Global Brain Science, Sendai 980-8575, Japan

Introduction

In the central nervous system (CNS) signals are transmitted from neuron to neuron at synapses. Synapses are also the principal sites of short- and long-term changes of neuronal networks. In the hippocampus, the axon of a dentate granule cell (mossy fiber, MF) provides robust excitatory inputs on 11–18 CA3 pyramidal cells at their proximal dendrites [1, 2]. Each transmission is mediated by a large MF bouton (LMFB), which forms a complex of tens of excitatory synapses. The MF-CA3 transmission is also highly dynamic over a large range during short- and long-term plasticity. These peculiar morphological and physiological features led to the proposal that the MF input might be involved in filtering out context for building the complete episodic memory [3]. Pharmacological studies using β-phorbol esters (BPE), synthetic analogues of diacylglycerol (DAG), one of the signaling messengers produced by phospholipases, showed that they induced the potentiation of transmission in many kinds of synapses through activating the C_1 domain-containing receptors [4, 5]. The BPEs are amongst the most potent in up-regulating the transmission at the MF-CA3 synapse, suggesting that the DAG/BPE-dependent cascade is involved in the plasticity of this synapse [6–10]. However, their effects on synaptic vesicle exocytosis have not yet been investigated.

The inside of a secretory vesicle is acidic (pH 5.6), whereas it becomes neutral (pH 7.4) instantaneously upon exocytosis [11]. The intravesicular change of pH is optically detected by a fluorescence change of a pH-sensitive

derivative of green fluorescent protein (pHluorin) when it is expressed inside the secretory vesicles by fusing to the lumenal domain of a vSNARE-type vesicular membrane protein synaptobrevin/VAMP-2 [11–13]. In this paper we optically evaluated the exocytosis-dependent changes of fluorescence from individual LMFBs in acute hippocampal slices from transgenic mice that express this fusion protein (synaptopHluorin, SpH) only in the MF boutons [14]. We found that one of the BPEs, 4β-phorbol 12,13-diacetate (PDAc) enhanced the activity-dependent SpH response in a single LMFB without influencing the SpH recycling rate. This effect of PDAc was almost completely blocked by staurosporine, which inhibits a broad spectrum of protein kinases at their ATP-binding sites, but not the non-PKC C_1 domain-containing receptors. It is suggested that BPEs enhance the activity-dependent exocytosis of synaptic vesicles through mechanisms involving protein kinases.

Methods

Hippocampal slice preparation

The experiments were carried out using 14–21-day-old heterozygous mice from one of the thy-1 promotor-synaptopHluorin (SpH) transgenic lines with the background of C57BL/6, TV-42, RIKEN BRC, acc. no. 01519 (http://www.brc.riken.jp/lab/animal/en/), which express SpH selectively in the mossy fiber (MF) boutons of the hippocampus [14]. The mice were decapitated under ether-anesthesia, and hippocampal slices (300–400 μm) were prepared as described [15]. For the dissection, a cutting solution containing (in mM) 229 mannitol, 3 KCl, 26 $NaHCO_3$, 1 H_3PO_4, 7 $MgCl_2$, 0.2 lidocaine HCl, pH 7.4 (0°C) with 95% O_2 and 5% CO_2 mixed gas was used. Experiments were done at 23–25°C, while the slices were superfused (2 ml/min) with artificial cerebrospinal fluid (ACSF) containing (in mM) 114 NaCl, 2.5 KCl, 26 $NaHCO_3$, 1 NaH_2PO_4, 10 mannitol, 2.5 $CaCl_2$, 1.3 $MgCl_2$, 10 glucose (pH 7.4 with 95% O_2 and 5% CO_2 mixed gas). All animal procedures were conducted in accordance with the guiding principles of the Physiological Society of Japan and NIH.

Extracellular recordings

Field excitatory postsynaptic potentials (fEPSPs) were recorded in the stratum lucidum of the CA3 region using glass microelectrodes with a pipette resistance of 0.7–2 MΩ filled with 1.75% Na_2SO_4 solution. A tungsten bipolar stimulating electrode was placed in the dentate hilus, and two electrical pulses (200 μs duration, 150–250 μA intensity, 100 ms inter-stimulus interval) were

delivered intermittently every 30 s. At the end of the experiments, we examined the sensitivity of fEPSP to either 1 μM DCG-IV or 10 μM L-CCG-1, an agonist for the group-II metabotropic glutamate receptors, which are selectively expressed in the MF presynaptic terminals [16, 17]. Although the MF synaptic transmission is only slightly attenuated by these drugs after β-phorbol ester-induced potentiation [18], a reduction of fEPSPs was actually observed in the range of 10–60%. Recordings were made with a Gene Clamp amplifier (Axon Instruments, Foster City, CA) and amplified and filtered at 10 kHz with an FLA-01 amplifier (Cygnus Technology, Inc., Delaware Water Gap, PA), digitized at 20 kHz with a DigiData 1320 A/D converter (Axon Instruments). Data were analyzed with Clampfit 9.2 software (Axon Instruments).

Optical imaging of exocytosis

SpH was excited with an argon laser at 488 nm, and fluorescence was collected through a 505-nm long-pass filter under conventional confocal microscopy equipped with a 63× 0.95 NA objective (LSM 510 META, Carl Zeiss, Oberkochen, Germany). Individual MF boutons were identified in the stratum lucidum of acute slices of hippocampus by SpH fluorescence (Fig. 1a, b) as some SpH molecules are distributed in the plasma membrane [13, 14, 19]. Throughout every experiment the fluorescence intensity of a region of interest (ROI) was measured with fixed sensitivity and was expressed in arbitrary fluorescence units (AFU), while the laser power was also set at a fixed intensity. The sampling frequency of images was set at 2 Hz (Figs. 1, 2, 3, 4c, and 5) or 1 Hz (Fig. 4a). Since only a small subset of LMFBs was responsive to the MF stimulation, they were detected by the following protocol. The LMFBs were electrically stimulated at 10 Hz for 10 s, while confocal images (512 × 512 pixels) were sampled (Fig. 1c, d). To identify the LMFBs, three bright fluorescent spots in the same focal plane were used as landmarks. Once one of the landmarks went out of focus, the experiment was no longer included in the analysis. Both baseline and responsive images were median-filtered at 5 pixels, and the difference image was calculated by subtracting the baseline image from the response image (Supplementary movie). Subsequently, the difference image was median-filtered at 8 pixels, and the signals derived from small-sized boutons or non-specific intrinsic fluorescence was largely removed. Each spot with brightness greater than a threshold of 10 AFU was defined as a responsive LMFB (Fig. 1e). Circular ROIs of 2.24-μm diameter were set at the responsive LMFBs, and the time series data of ROIs were acquired from raw image stacks. At least ten other ROIs were also set at non-responsive MF regions of the same image, and the background fluorescence changes were recorded. The background fluorescence changes, which
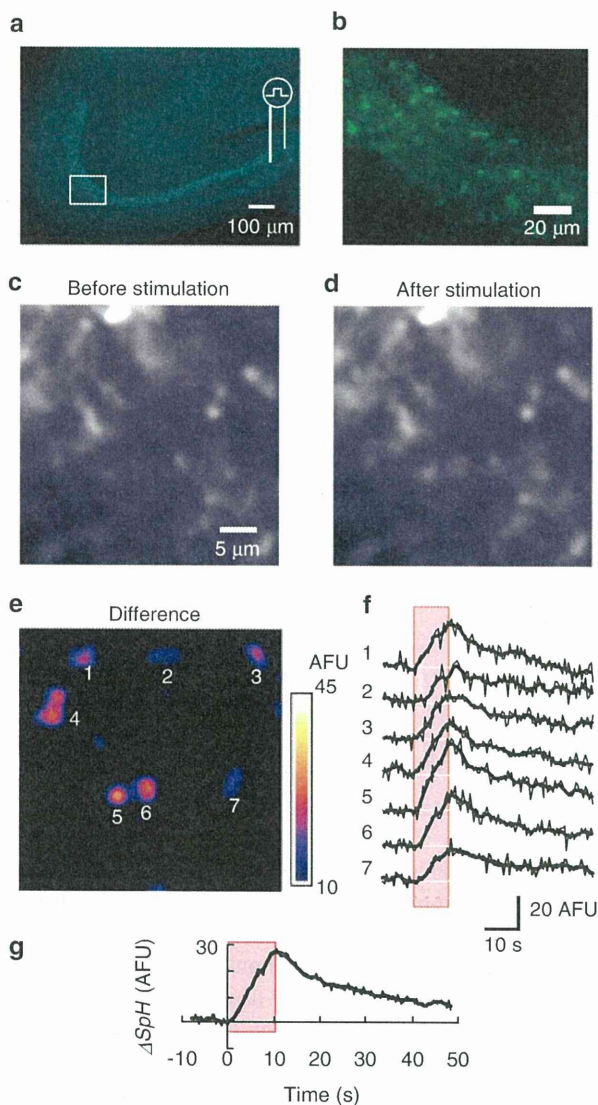
Fig. 1 Synaptic vesicle dynamics in individual large MF boutons (LMFBs) in the hippocampus. **a** A synaptopHluorin (SpH) fluorescence image of an acute slice of TV-42 transgenic mouse hippocampus. The MFs were stimulated at the dentate hilus (*right*) and recorded from the distal CA3 region (*left square*). **b** An enlarged view of the stratum lucidum included in the square in **a**. Individual LMFBs are identifiable by the SpH fluorescence in the plasma membrane. **c** A sample averaged image of the SpH fluorescence of LMFBs before nerve stimulation. **d** Similar to **c**, but the images were sampled near the end of repetitive stimulation of 10 Hz for 10 s. **e** The digital subtraction of both images (difference image). The magnitude is shown as a pseudocolor rating. **f** Time-dependent profiles of SpH fluorescence signals of the ROIs indicated in **e**. The stimulation period is indicated by a red stripe. **g** Average SpH signal profile of sample records in **f**. Note that the fluorescence intensity steadily increased during repetitive stimulation, but recovered to the baseline after the cessation of stimulation

were mainly derived from the fluorescence bleaching, were averaged, normalized to the value at time 0 (the normalized background fluorescence). For each ROI the effect of

fluorescence bleaching was removed by dividing the SpH florescence value by the normalized background fluorescence value of the same time point. The time-dependent change of the SpH fluorescence intensity was thus obtained for each ROI (Fig. 1f, thin lines). These ratio data were also digitally filtered by applying a weighted moving-average protocol as described [15] (Fig. 1f, thick lines). The weights, 0.080251, 0.137137, 0.182615, 0.2, 0.182615, 0.137137 and 0.080251, were designed by the Kaiser window finite impulse response (FIR) algorithm so that the sum of the squares of errors was minimized, while the sum of the weights was equal to 1. The mean noise amplitude was calculated as the average of the absolute difference between the raw ratio data and the filtered ratio data. The signal range was calculated by subtracting the minimal filtered ratio value during another 10 s just before stimulation from the maximal filtered ratio value during 10-s repetitive stimulation. The signal-to-noise ratio (S/N) was thus obtained by dividing this signal range by the mean noise amplitude. If S/N < 5, the data were not employed for the subsequent analyses. The time-dependent change of the ratio data (ΔSpH) was obtained by subtracting the minimal filtered ratio value from the ratio data. In the following figures showing the ΔSpH, the thin lines represent ratio data before filtering and the thick lines those after filtering. Averaged ΔSpH are also shown as in Fig. 1g. Image analysis was performed with ImageJ software (http://rsb.info.nih.gov/ij/), and the time series data of ROIs were sampled in digits and analyzed with Excel software (Microsoft, USA) and R software (http://cran.r-project.org/).

Chemicals

Pharmacological reagents were bath-applied in the recording chamber (2 ml) at a constant flow rate (2 ml/min). Reagents used in this study and their sources were as follows: kynurenic acid (Sigma-Aldrich, St. Louis, MO), lidocaine HCl (Sigma-Aldrich), (2S,2'R,3'R)2-(2',3'-dicarboxycyclopropyl)glycine (DCG-IV, Tocris Cookson, Bristol, UK); (2S,1'S,2'S)-2-(2-carboxycyclopropyl)glycine (L-CCG-1, Tocris), bafilomycin A1 (Wako, Osaka, Japan); 4β-phorbol 12,13-diacetate (PDAc, Wako); 4α-phorbol (Sigma-Aldrich); staurosporine (Sigma-Aldrich). Bafilomycin A1 was dissolved in DMSO containing 20% pluronic acid, then diluted. PDAc, 4α-phorbol and staurosporine were dissolved in DMSO, then diluted. Stocks of these were preserved at −20°C.

Statistical analysis

Values are expressed as mean ± SEM (number of experiments) unless otherwise noted. Statistical significance was tested by the Wilcoxon signed-ranks test for paired data

Fig. 2 Ca^{2+} sensitivity of ΔSpH. **a** Sample records of fEPSP evoked by a two-pulse protocol (interval, 100 ms) at 0.033 Hz in an ACSF containing $[Ca^{2+}]_o$ at 2.5 mM (*top trace*), 5 mM (*middle trace*) or 0 mM (*bottom trace*). **b** $[Ca^{2+}]_o$ dependence of fEPSP ($n = 8$ slices). **c** Sample records of ΔSpH from a LMFB by a train of repetitive stimulation (10 Hz for 10 s); $[Ca^{2+}]_o$ at 2.5 mM (*top trace*), 5 mM (*middle trace*) or 0 mM (*bottom trace*). **d** $[Ca^{2+}]_o$ dependence of ΔSpH ($n = 12$ boutons, 3 slices)
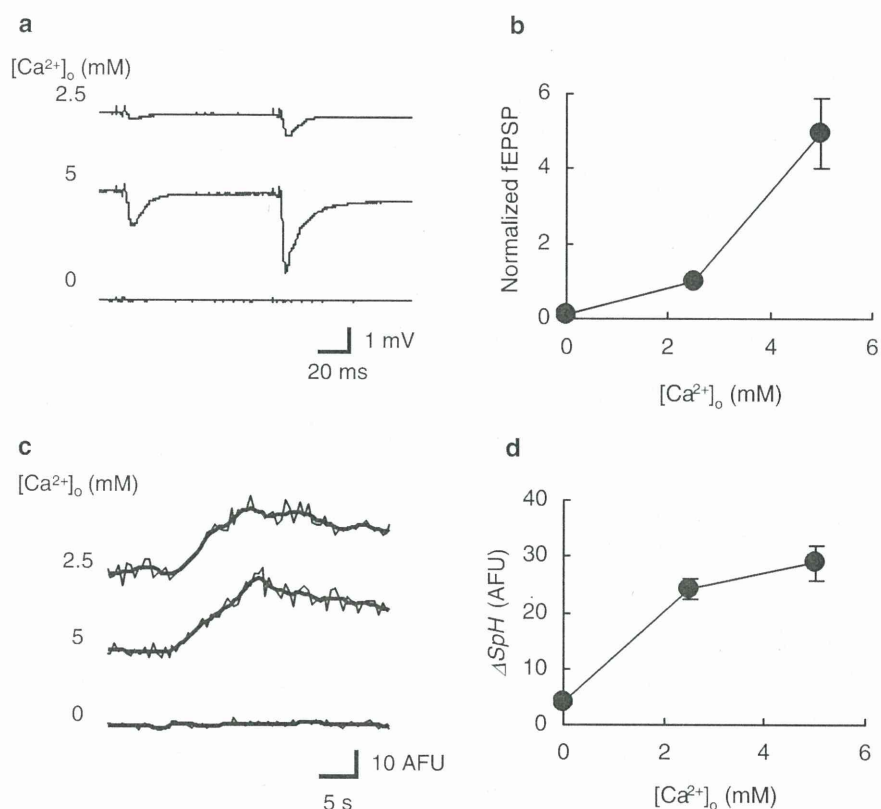

Results

Ca^{2+}-sensitivity of ΔSpH

In this study we measured the basal synaptic transmission using the first fEPSPs of paired stimuli at 0.033 Hz. On the other hand, the ΔSpH is the cumulative response to the repetitive stimulation (10 Hs for 10 s). The first fEPSP is dependent on the size of the readily releasable pool (RRP), where the vesicles are docked/primed to the active zone membrane at each synapse [20–22] and the vesicle fusion probability (see Appendix). During repetitive stimulation at 10 Hz, the vesicular exocytosis is in equilibrium with the vesicle replenishment from the reserve subpopulation of vesicle pool [23] because of the relatively small size of RRP [15, 24]. Therefore, the ΔSpH is expected to be more dependent on the vesicle replenishment than the RRP. To test this, the effects of vesicle fusion probability were investigated by changing $[Ca^{2+}]_o$. When $[Ca^{2+}]_o$ was increased from 2.5 mM ($[Mg^{2+}]_o$, 2.5 mM) to 5 mM ($[Mg^{2+}]_o$, 0 mM), the fEPSP amplitude was enhanced by

4.94 ± 0.93-fold ($n = 8$ slices) (Fig. 2a). This enhancement was accompanied with the reduction of paired-pulse ratio from 3.04 ± 0.26 to 2.08 ± 0.11 ($n = 8$ slices). In summary, the fEPSP followed a nonlinear relationship with $[Ca^{2+}]_o$ (Fig. 2b). On the other hand, the ΔSpH was less sensitive to the same change of $[Ca^{2+}]_o$ (Fig. 2c). The mean ΔSpH was 22.3 ± 1.3 AFU at 2.5 mM $[Ca^{2+}]_o$ and 25.8 ± 1.8 AFU at 5 mM $[Ca^{2+}]_o$ with significant difference ($n = 24$ boutons, 6 slices, $P < 0.05$ Wilcoxon signed-ranks test). Since the ΔSpH was undetectable when $[Ca^{2+}]_o$ was 0 mM ($[Mg^{2+}]_o$, 5 mM; EGTA, 1 mM), its relationship to $[Ca^{2+}]_o$ was different from that of fEPSP in the $[Ca^{2+}]_o$ sensitivity (Fig. 2d). These results are consistent with the notion that the first fEPSP and the ΔSpH are distinct in their aspects of the exocytosis.

BPE-dependent enhancement of ΔSpH

Previously, it was shown that the fEPSP is augmented by PDAc at the stratum lucidum of the hippocampus at the concentration of 0.5–10 μM [6, 7, 9, 10, 18]. This was also the case in the present study, and the fEPSP was potentiated by 10 μM PDAc to, on average, $533 \pm 64\%$ ($n = 8$ slices) of control (Fig. 3a, filled circles). On the other hand, the PDAc treatment did not affect the amplitude of the fiber volley response preceding the fEPSP, which is an indication

and by the Mann–Whitney U-test or the Kolmogorov–Smirnov test for unpaired data. The significance limit was set at $P = 0.05$ in any test.

Fig. 3 Enhancement of the activity-dependent increment of SpH fluorescence (ΔSpH) by β-phorbol esters (BPE). **a** The fEPSP was monitored at 0.033 Hz using a two-pulse protocol (insets left, before and right, after PDAc); the peak amplitude of the first fEPSP (*filled circles*, mean ± SEM, n = 8 slices) and the fiber volley amplitude (*open diamonds*, mean ± SEM, n = 3 slices). Each data was normalized to the mean of five values preceding the sampling 1. The *numbered red double lines* indicate image sampling 1 and 2 when repetitive stimulations were applied at 10 Hz for 10 s. Drugs were bath-applied for the indicated periods. **b** The difference images of the same region before (*left*, sampling 1) and after PDAc (10 μM) (*right*, sampling 2). **c** The sample ΔSpH traces during MF stimulation of three LMFBs in **b** (indicated by *white arrows*) are compared before (sampling 1, *black*) and after PDAc (sampling 2, *blue*). **d** In some LMFBs, the negligibly small ΔSpH before (sampling 1, *black*) became obvious after PDAc (sampling 2, *blue*). **e** Each LMFB was plotted two-dimensionally to the sampling-1 (control) and the sampling-2 (test) values of ΔSpH; vehicle alone (*open circles*, n = 31 boutons, 5 slices), 4α-phorbol (*yellow squares*, n = 30 boutons, 6 slices) and PDAc (*blue diamonds*, n = 65 boutons, 10 slices). The *magenta line* shows that both are equal. **f** Cumulative probability plots of the ratio value of the ΔSpH at sampling 2 divided by that at sampling 1 (ratio-2/1 of ΔSpH); vehicle alone (*black line*), 4α-phorbol (*gray line*) and PDAc (*blue line*)
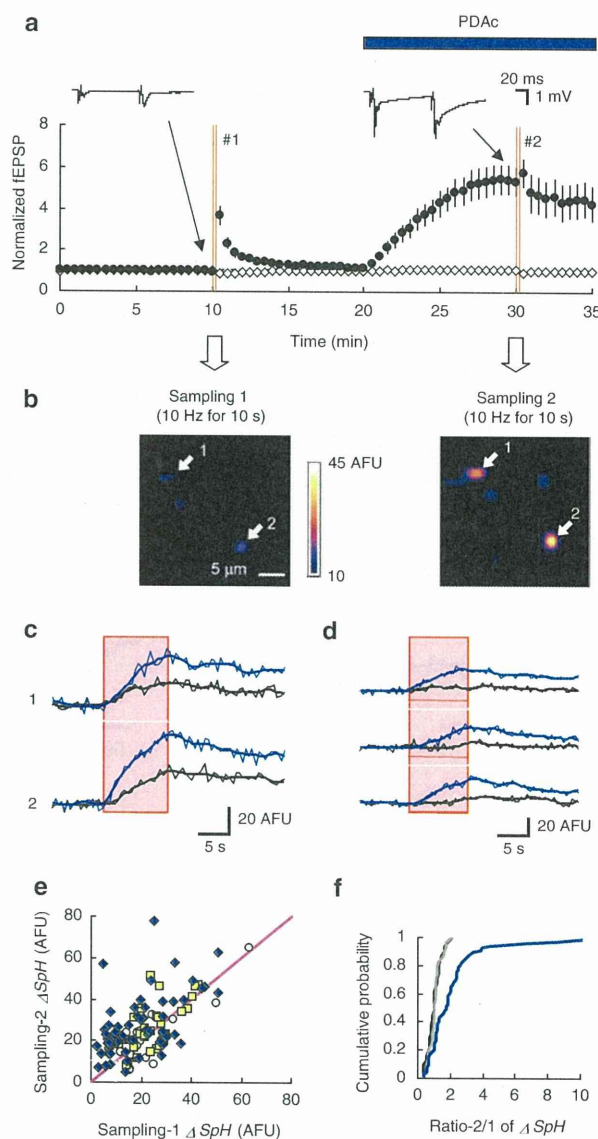
of the number of stimulated axons (open diamonds, mean 110 ± 4%, n = 3 slices). As shown in the Fig. 3a insets, the PDAc treatment significantly reduced the paired-pulse ratio from 2.1 ± 0.14 to 1.2 ± 0.03 (n = 8 slices, $P < 0.01$, Wilcoxon signed-ranks test), suggesting the involvement of presynaptic mechanisms [10]. The SpH images were sampled twice before (Fig. 3a, red double line no. 1) and after PDAc treatment (red double line no. 2). Figure 3b shows representative ΔSpH images (10 Hz for 10 s) before (left, sampling 1) and after (right, sampling 2) the treatment with PDAc. The PDAc treatment obviously enhanced the ΔSpH in some LMFBs (white arrows) as shown in the sample records in Fig. 3c. The effects of PDAc on the individual MF boutons were variable from bouton to bouton, and the boutons that responded to the repetitive stimulation with negligibly small ΔSpH often became obvious after PDAc (Fig. 3d). Figure 3e summarizes the effects of PDAc in which the ΔSpH values at sampling 2 were plotted to those at sampling 1 (blue diamonds, n = 65 boutons, 10 slices). The maximal ΔSpH at the end of a train of stimulation was 18.3 ± 1.5 AFU at sampling 1 and 26.5 ± 1.7 AFU at sampling 2, and the difference was significant ($P < 0.0001$, Wilcoxon signed-ranks test). We also plotted in the same figure the effects of the vehicle (DMSO) alone (white circles, n = 31 boutons, 5 slices, 22.0 ± 2.0 AFU at sampling 1 and 21.2 ± 1.9 AFU at sampling 2) and those of 4α-phorbol (10 μM), one of the inactive phorbol esters (yellow square, n = 30 boutons, 6 slices, 25.5 ± 1.5 AFU at sampling 1 and 27.1 ± 2.0 AFU at sampling 2). The ΔSpH at sampling 2 was virtually unchanged from that at sampling 1 by these control treatments. The effects of PDAc were more clearly shown by

comparing the ratio value of the ΔSpH at sampling 2 divided by that at sampling 1 (ratio-2/1 of ΔSpH) in cumulative probability plots (Fig. 3f). Although the PDAc significantly enhanced the ΔSpH ($P < 0.0005$, Kolmogorov–Smirnov test), the effects of 4α-phorbol were indistinguishable from the vehicle alone control. This is consistent with the notion that the 4α-phorbol esters are biologically inactive [4] and that the PDAc-dependent enhancement of the ΔSpH appeared to be specific to the C_1 domain-containing receptors such as PKC and Munc13s [4, 5, 25].

Evaluation of SpH recycling

After fusion, the SpH molecules in the vesicular membrane are exposed to the extracellular space (pH 7.4) and
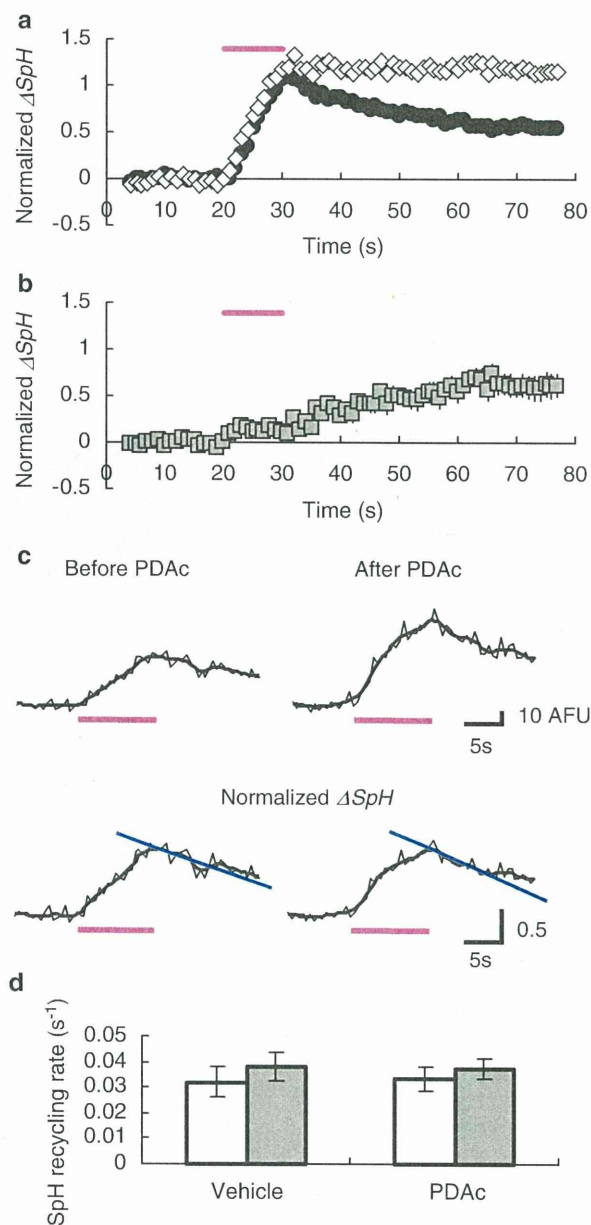
Fig. 4 Effects of BPE on the rate of SpH recycling. **a** The ΔSpH signals were normalized and averaged before (*closed circles*) and after 5 μM bafilomycin A1 (*open diamonds*) (mean ± SEM, $n = 30$ boutons, 7 slices). **b** The contribution of SpH recycling through the processes of endocytosis-reacidification was estimated by the subtraction of the ΔSpH before bafilomycin A1 from that after, and was plotted (*gray squares*, mean ± SEM, $n = 30$ boutons, 7 slices). **c** Each ΔSpH signal before (*top left*) and after PDAc (*top right*) was normalized to the value at the end of a train of repetitive stimulations (*bottom traces*) and a regression line (*blue*) was fitted to the data of 0–5 s after the last stimulation. **d** Summary (mean ± SEM) of the SpH recycling rate before (*open columns*) and after vehicle alone (DMSO, *left filled column*, $n = 27$ boutons, 4 slices) or PDAc (*right filled column*, $n = 44$ boutons, 10 slices)
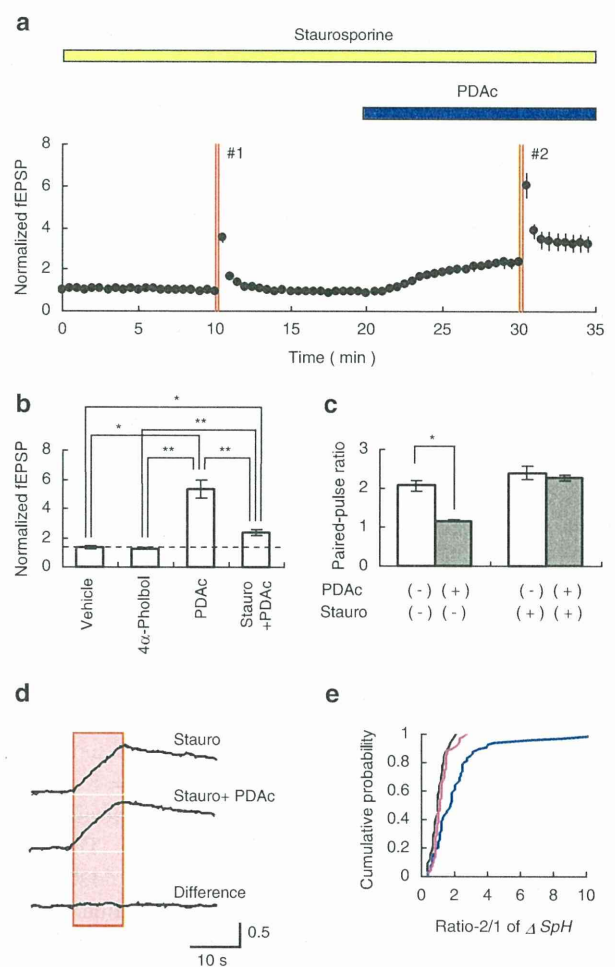

Fig. 5 Effects of staurosporine. **a** The effects of PDAc on fEPSPs in the presence of 1 μM staurosporine. The *numbered double lines* indicate image sampling 1 and 2. Reagents were bath-applied for the indicated periods. **b** Summary of the effects on the first fEPSP amplitude of the treatments: vehicle alone (*first left*, $n = 5$ slices), 4α-phorbol (*second left*, $n = 7$ slices), PDAc (*third left*, $n = 8$ slices) and staurosporine plus PDAc (*right most*, $n = 12$ slices). *$P < 0.01$ and **$P < 0.0005$ (Mann–Whitney U-test). **c** Summary of the effects of PDAc on the paired-pulse ratio of fEPSPs in the absence (*left*, $n = 8$ slices) and the presence of staurosporine (*right*, $n = 12$ slices). *Open column*, paired-pulse ratio before PDAc treatment; closed column, 10 minutes after exposure to PDAc. *$P < 0.01$ (Wilcoxon signed-ranks test). **d** Average fluorescence profiles of LMFBs ($n = 65$ boutons, 15 slices) in the presence of staurosporine before (*top*), after PDAc (*middle*) and the difference (*bottom*). **e** Cumulative probability plots of the ratio-2/1 value of ΔSpH; vehicle alone (*black line*), PDAc (*blue line*) and staurosporine plus PDAc (*magenta line*)

de-protonated to become fluorescent [11–13]. The synaptic vesicles are then recycled into a vesicular pool, refilled with transmitter and reutilized for the following transmission [22, 26]. The SpH molecules are retrieved from the

plasma membrane with the new vesicles during the process of endocytosis and are protonated to become non-fluorescent with the progress of the reacidification of the intravesicular space by the activity of V-type H^+ ATPase [19, 27]. Therefore, the rising phase of the ΔSpH represents the difference between the exocytosis and the molecule's recycling through the process of endocytosis-reacidification, whereas the falling phase kinetics are solely dependent on the recycling [15, 27, 28]. The PDAc can enhance the ΔSpH either through increasing the exocytosis rate or through decreasing the recycling rate.

When the intravesicular reacidification is completely blocked by bafilomycin A1, a potent inhibitor of the V-type H^+ ATPase [13, 15], the recycling vesicles are expected to be trapped in alkaline. To evaluate the contribution of the recycled SpH, the ΔSpH was normalized to the value at the end of the train stimulation (10 Hz for 10 s) in the absence of bafilomycin A1, and the effects of bafilomycin A1 were examined as shown in Fig. 4a. As expected the falling rate of the SpH response was almost null in the presence of 5 μM bafilomycin A1. Therefore, the contribution of recycled SpH was estimated by subtraction of the ΔSpH before bafilomycin A1 from that after (Fig. 4b). This bafilomycin A1-sensitive component steadily increased during the train stimulation, and was $10 \pm 6\%$ ($n = 30$ boutons, 7 slices) at the end of the train stimulation. The bafilomycin A1-sensitive component was again examined in the presence of PDAc, was $16 \pm 8\%$ ($n = 26$ boutons, 3 slices), and was insignificantly different from the value in the absence ($P > 0.5$, Mann–Whitney U-test).

The recycling rate of SpH during the train stimulation can also be approximated by the initial rate of the fluorescence reduction after the last stimulation (Fig. 4b) [28]. As the first step, the filtered ΔSpH was normalized to the value at the end of the train stimulation (10 Hz for 10 s). Next, a regression line was fitted to the data of 0–5 s after the last stimulation, and its slope was adopted as the SpH recycling rate (Fig. 4c). As shown in Fig. 4d, the effects of PDAc on the SpH recycling rate were almost negligible and were similar to the effects of vehicle alone ($P > 0.5$, Mann-Whitney U-test).

Taken together, there was no evidence that PDAc decreased the SpH recycling rate. The PDAc-dependent enhancement of the SpH response is well attributable to the change of the exocytosis rate.

Effects of staurosporine

Since the SpH response was specifically enhanced by PDAc, but not by 4α-phorbol, the PDAc-dependent enhancement of the SpH response appeared to be specific to the C_1 domain-containing receptors such as PKC and Munc13s [4, 5, 25]. To investigate the downstream mechanisms of BPE, we examined the effects of staurosporine, which inhibits a broad spectrum of protein kinases at their ATP-binding sites [29, 30]. As shown in Fig. 5a, the PDAc potentiated the fEPSP to a mean $232 \pm 20\%$ ($n = 12$ slices) of control in the presence of staurosporine (1 μM). Although the magnitude of this potentiation was significantly smaller than in the absence of staurosporine ($P < 0.0001$, Mann–Whitney U-test), it was still significantly greater than the control (vehicle alone and 4α-phorbol treatments, $P < 0.01$, Mann–Whitney U-test) (Fig. 5b). During the PDAc-induced fEPSP potentiation, the paired-pulse ratio was always decreased from its initial value. However, this was not the case in the presence of staurosporine (Fig. 5c), and the paired-pulse ratio was on average 2.3 ± 0.09 ($n = 12$ slices), which is insignificantly different from the control (2.4 ± 0.17, Wilcoxon signed-ranks test).

As shown in Fig. 5d, the average profiles of the ΔSpH ($n = 65$ boutons, 15 slices) were compared before and after PDAc (10 μM), while the slices were pretreated with staurosporine (1 μM). The maximal ΔSpH at the end of a train of stimulation was 26.7 ± 1.3 AFU at sampling 1 and 26.4 ± 1.4 AFU at sampling 2, and the difference was insignificant ($P > 0.7$, Wilcoxon signed-ranks test). The subtracted curve (difference) indicates that PDAc was almost ineffective on the ΔSpH in the presence of staurosporine. Figure 5e shows the cumulative probability plots of the ratio-2/1 values of ΔSpH. The effects of PDAc were almost completely blocked by staurosporine ($P < 0.0001$, Kolmogorov–Smirnov test) and indistinguishable from the vehicle alone control. The staurosporine-sensitive cascade appears to be one of the major downstream reactions of PDAc in the case of exocytosis during repetitive activation of the LMFBs. This is in contrast to the case of intermittent synaptic transmission (e.g., 0.033 Hz) where a significant potentiation remained even in the presence of staurosporine.

Discussion

The BPEs, such as 4β-phorbol-12,13-dibutyrate (PDBu, 10 μM) and PDAc (2 μM), increased the MF-dependent population spike with negligible effects on the glutamate sensitivity [6]. The PDAc increased the quantum content with little changes in the quantum size [7], and its potentiation was accompanied by a reduction of the paired-pulse ratio [10]. In the present study the PDAc-dependent enhancement of fEPSP was not accompanied by an enhancement of the fiber volley response as previously noted [18], suggesting the up-regulation of synaptic transmission. These lines of electrophysiological evidence suggest that the BPEs would enhance the quantal

transmitter release from the LMFBs. However, the validity of this interpretation has to be re-investigated taking into consideration the nonuniform probability of release, the concentration of glutamate in the synaptic cleft, the effects of the rapid desensitization of the glutamate AMPA receptors and the unsilencing of postsynaptic responsiveness [31–36]. This paper presents additional evidence in a more direct way that the BPEs enhance the exocytosis in a single LMFB in acute hippocampal slices using the SpH transgenic mice. The ΔSpH was enhanced on average 2.2-fold by the PDAc (10 μM), although the magnitude of potentiation was variable from bouton to bouton. On the other hand, its effect on the recycled component of ΔSpH, which is regulated by the endocytosis and the subsequent reacidification of the vesicles, was negligible. Therefore, the PDAc-dependent change of the ΔSpH could be attributed to the change of the exocytosis rate. However, its effects on the endocytosis have to be further investigated since the synaptobrevin/VAMP-2, which can be detected by the SpH fluorescence, was retrieved from the plasma membrane in a way kinetically differentiated from other vesicle marker proteins, such as the synaptophysin and the vesicular glutamate transporters [37, 38].

It should be noted that our ΔSpH measurement evaluated a different aspect of exocytosis from the previous electrophysiological measurements of synaptic transmission. Since the ΔSpH showed small sensitivity to $[Ca^{2+}]_o$ between 2.5 and 5 mM, the contribution of the vesicle fusion probability is small. Rather, it could be dependent on the magnitude of the vesicle replenishment [15]. However, in the CA3-CA1 synapses of hippocampus, the SpH fluorescence change evoked by a train of repetitive stimulation (10 Hz for 5 s) is dependent on $[Ca^{2+}]_o$ (0.5–5 mM) like fEPSP [39]. It is possible that these two synapses are different in the $[Ca^{2+}]_o$–ΔSpH relationship, but the underlying mechanisms of this difference should be investigated in future.

Staurosporine-sensitive and -resistant mechanisms

DAG is a key messenger regulating the efficacy of synaptic transmission. The effects of DAG and its analogues, BPEs, are partly mediated by the activation of protein kinase C (PKC), which facilitates exocytosis in a wide variety of cells and presynaptic terminals [40–42]. They also regulate the efficacy of synaptic transmission through activating non-PKC C_1 domain-containing receptor proteins, such as Munc13s, which are presynaptic vesicle priming proteins [43–45]. It has been suggested that the PKC-dependent and Munc13-1-dependent pathways synergistically modulate the exocytosis [4, 5]. In this study the PDAc-dependent enhancement of the ΔSpH was almost completely blocked by staurosporine, one of the broad spectrum protein kinase

inhibitors. This suggests the involvement of some protein kinases in a cascade downstream of the C_1 domain-containing receptors. However, the effects of more specific inhibitors have to be studied to identify the key molecules. A previous study described that the PDAc-induced potentiation of MF synaptic transmission is partially antagonized by a PKC-selective inhibitor, bisindolylmaleimide I (BIS-I), but a BIS-I resistant component of potentiation remained [10]. However, we found that BIS-I and its derivatives, which differentiate PKC from other kinases, were strongly fluorescent at the SpH emission spectra when included in the cell. Therefore, it will be necessary in the future to study the possible involvement of PKC using mice in which one of PKC isoforms is knocked out [46] or RNAi-dependent knockdown of one of the PKC isoforms [47].

We also found that the basal synaptic transmission (e.g., 0.033 Hz) was still potentiated in the presence of staurosporine, whereas the effects on the ΔSpH, which is induced by a train of repetitive stimulation, were completely inhibited. Therefore, during a train of repetitive stimulation of LMFB, the response to the first stimulation, which is detectable by fEPSP, and the integrated exocytosis measured by the ΔSpH would be different in the sensitivity to staurosporine. The effects of staurosporine were almost quantitatively equivalent to those of BIS-I in the case of fEPSP. The PDAc (10 μM) treatment potentiated the fEPSP to $232 \pm 20\%$ of control in the presence of staurosporine, but to $533 \pm 64\%$ of control in the absence. The same treatment potentiated the fEPSP to $258 \pm 34\%$ in the presence of BIS-I [10]. Since the staurosporine-resistant component of potentiation was not accompanied by a reduction of the paired-pulse ratio, an indication of increased vesicle fusion probability (see Appendix), other mechanisms are suggested to be involved. The possibility should be investigated that the staurosporine-resistant fEPSP potentiation is accompanied by the enhancement of postsynaptic sensitivity to glutamate. The spatio-temporal changes of glutamate concentration are also under the regulation of the amount of transmitter release per vesicle, the speed of glutamate release, the synaptic cleft morphology and the speed of glutamate clearance from the synaptic cleft [48, 49]. The BPEs have been demonstrated to increase the RRP size in other synapses [50–52] as well as in the slow exocytosis of endocrine cells [53], although it remains undetermined whether these effects are actually PKC-dependent or not. Since the RRP is fractionally small in an LMFB [15, 24] and would be depleted in 10–20 action potentials if it is not replenished, its increase would hardly be detectable in our SpH study.

The presence of a staurosporine-resistant component of fEPSP potentiation suggests that the signaling cascade via the non-PKC C_1 domain-containing receptors is involved

in the facilitation of synaptic transmission through these mechanisms. Recently, it has been suggested that Munc13-1, one of the non-PKC C_1 domain-containing receptors, localized to active zones in the presynaptic terminal, may also be involved in the regulation of synaptic efficacy by BPEs [54–56]. When the DAG/BPE-binding site of Munc13-1 is genetically deficient or non-functional, the effects of BPEs are largely impaired [56, 57]. Although the present study did not prove whether BPEs potentiate MF synaptic transmission through Munc13-1, it does not conflict with the notion that the PKC-dependent and Munc13-1-dependent pathways synergistically modulate the exocytosis [4, 5].

The ΔSpH unsilencing

We found that the ΔSpH, which was negligibly small at sampling 1, become obvious at sampling 2 after the PDAc in some LMFBs. These synapses are possibly presynaptically silent or weak in the release ability before PDAc [34]. Alternatively, the transmitter release might be rapidly depressed during repetitive stimulation. These possibilities should be clarified in future studies, e.g., the simultaneous recordings of EPSC and SpH fluorescence. Recent studies using cultured networks of developing hippocampal neurons have described the presence of presynaptically silent synapses, which become transmittable through mechanisms dependent on cAMP-protein kinase A (PKA) or BDNF-Cdc signaling cascades [58–62]. At the CA3-CA1 synapses of the mouse hippocampus, the slow presynaptic component of long-term potentiation (LTP), which is detected by the change of SpH fluorescence, is mediated by the PKA and the L-type Ca^{2+} channels [39]. It is possible that some boutons are unsilenced in the ΔSpH. Since MF-LTP is dependent on the AC-PKA cascade [63, 64], it is probably accompanied with the increased ΔSpH. The unsilencing of ΔSpH might be related to the accumulation and organization of the large arrays of vesicular and non-vesicular molecules required for exocytosis as they are during synaptogenesis [65, 66]. PKC is one of the protein kinases involved in these processes. For example, PKC phosphorylates GAP-43, one of major proteins of the presynaptic and growth cone membrane, during synaptic potentiation [67]. Another PKC substrate is myristoylated alanine-rich C kinase substrate (MARCKS), which is involved in both synaptic maturation and the synaptic plasticity [68, 69].

In the hippocampus of a living animal the signals are usually a train of impulses of variable frequencies [70], sometimes at around 10 Hz (a theta rhythm) [71, 72]. When DAG/BPEs facilitate the fusion probability by increasing the Ca^{2+} influx and the Ca^{2+} sensitivity of exocytosis [10], they up-regulate the transmission efficacy

for impulses arriving early in a train, but down-regulate it for impulses arriving later because of the depletion of RRP. This effect could explain the reduction of the paired-pulse ratio. Even if the RRP were to be increased, the potentiation should be transient if it is not replenished. On the other hand, the staurosporine-sensitive enhancement of exocytosis followed a more prolonged time course. Therefore, the DAG/BPE-dependent signaling cascade is suggested to be involved in the facilitation of the vesicle replenishment through a staurosporine-sensitive mechanism and to maintain the fidelity of transmission at a high level during a train of repetitive firings of the presynaptic neuron.

Appendix

Reduction of the paired-pulse ratio

According to the quantal hypothesis [36, 73], a postsynaptic response (E) is related to the following relationship.

$$E = Npq, \tag{1}$$

where q is the postsynaptic response by a single quantum (quantal size). The meanings of N and p are definition-dependent. If p is regarded as the probability of vesicle fusion to the plasma membrane, then N refers to the number of vesicles drawn from the next action potential, the readily releasable pool (RRP) or the release-ready pool [20–22]. On the other hand, if p is regarded as the release probability of a release site, N should be the number of release sites, the morphological correlates of which are the number of active zones of a presynaptic terminal. When a presynaptic axon is stimulated by two pulses of a short interval, the vesicle fusion probability by the second action potential (p') is generally increased by some mechanisms dependent on the residual Ca^{2+} [74–78]. On the analogy of the Eq. 1, the second postsynaptic response (E') will be expressed as,

$$E' = \{N(1 - p) + R\}p'q'. \tag{2}$$

Here, R is the number of vesicles replenished to the RRP during the interval between the first and the second action potentials, and q' is the quantal size of the second response.